

KINGFISH – Key Insights on Nearby Galaxies: A Far-Infrared Survey with *Herschel*: Survey Description and Image Atlas¹

R. C. Kennicutt¹, D. Calzetti², G. Aniano³, P. Appleton⁴, L. Armus⁵, P. Beirão⁵, A. D. Bolatto⁶, B. Brandl⁷, A. Crocker², K. Croxall⁸, D. A. Dale⁹, J. Donovan Meyer¹⁰, B. T. Draine³, C. W. Engelbracht¹¹, M. Galametz¹, K. D. Gordon¹², B. Groves^{7,16}, C.-N. Hao¹³, G. Helou⁴, J. Hinz¹¹, L. K. Hunt¹⁴, B. Johnson¹⁵, J. Koda¹⁰, O. Krause¹⁶, A. K. Leroy¹⁷, Y. Li², S. Meidt¹⁶, E. Montiel¹¹, E. J. Murphy¹⁸, N. Rahman⁶, H.-W. Rix¹⁶, H. Roussel¹⁵, K. Sandstrom¹⁶, M. Sauvage¹⁹, E. Schinnerer¹⁶, R. Skibba¹¹, J. D.T. Smith⁸, S. Srinivasan¹⁵, L. Vigroux¹⁵, F. Walter¹⁶, C. D. Wilson²⁰, M. Wolfire⁶, S. Zibetti²¹

¹Institute of Astronomy, University of Cambridge, Madingley Road, Cambridge CB3 0HA, UK

²Department of Astronomy, University of Massachusetts, Amherst, MA 01003, USA

³Department of Astrophysical Sciences, Princeton University, Princeton, NJ 08544, USA

⁴NASA Herschel Science Center, IPAC, California Institute of Technology, Pasadena, CA 91125, USA

⁵Spitzer Science Center, California Institute of Technology, MC 314-6, Pasadena, CA 91125, USA

⁶Department of Astronomy, University of Maryland, College Park, MD 20742, USA

⁷Leiden Observatory, Leiden University, P.O. Box 9513, 2300 RA Leiden, The Netherlands

⁸Department of Physics and Astronomy, University of Toledo, Toledo, OH 43606, USA

⁹Department of Physics & Astronomy, University of Wyoming, Laramie, WY 82071, USA

¹⁰Department of Physics and Astronomy, SUNY Stony Brook, Stony Brook, NY 11794-3800, USA

¹¹Steward Observatory, University of Arizona, Tucson, AZ 85721, USA

¹²Space Telescope Science Institute, 3700 San Martin Drive, Baltimore, MD 21218, USA

¹³Tianjin Astrophysics Center, Tianjin Normal University, Tianjin 300387, China

¹⁴INAF - Osservatorio Astrofisico di Arcetri, Largo E. Fermi 5, 50125 Firenze, Italy

¹⁵Institut d'Astrophysique de Paris, UMR7095 CNRS, Université Pierre & Marie Curie, 98 bis Boulevard Arago, 75014 Paris, France

¹⁶Max-Planck-Institut für Astronomie, Königstuhl 17, D-69117 Heidelberg, Germany

¹⁷National Radio Astronomy Observatory, 520 Edgemont Road, Charlottesville, VA 22903, USA

¹⁸Observatories of the Carnegie Institution for Science, 813 Santa Barbara Street, Pasadena, CA 91101 USA

¹⁹CEA/DSM/DAPNIA/Service d'Astrophysique, UMR AIM, CE Saclay, 91191 Gif sur Yvette Cedex

²⁰Department of Physics & Astronomy, McMaster University, Hamilton, Ontario L8S 4M1, Canada

²¹DARK Cosmology Centre, Niels Bohr Institute, University of Copenhagen, Juliane Maries Vej 30, DK-

ABSTRACT

The KINGFISH project (Key Insights on Nearby Galaxies: a Far-Infrared Survey with *Herschel*) is an imaging and spectroscopic survey of 61 nearby ($d < 30$ Mpc) galaxies, chosen to cover a wide range of galaxy properties and local interstellar medium (ISM) environments found in the nearby Universe. Its broad goals are to characterize the ISM of present-day galaxies, the heating and cooling of their gaseous and dust components, and to better understand the physical processes linking star formation and the ISM. KINGFISH is a direct descendant of the *Spitzer* Infrared Nearby Galaxies Survey (SINGS), which produced complete *Spitzer* imaging and spectroscopic mapping and a comprehensive set of multi-wavelength ancillary observations for the sample. The *Herschel* imaging consists of complete maps for the galaxies at 70, 100, 160, 250, 350, and 500 μm . The spectral line imaging of the principal atomic ISM cooling lines ([OI]63 μm , [OIII]88 μm , [NII]122,205 μm , and [CII]158 μm) covers the subregions in the centers and disks that already have been mapped in the mid-infrared with *Spitzer*. The KINGFISH and SINGS multi-wavelength datasets combined provide panchromatic mapping of the galaxies sufficient to resolve individual star-forming regions, and tracing the important heating and cooling channels of the ISM, across a wide range of local extragalactic ISM environments. This paper summarizes the scientific strategy for KINGFISH, the properties of the galaxy sample, the observing strategy, and data processing and products. It also presents a combined *Spitzer* and *Herschel* image atlas for the KINGFISH galaxies, covering the wavelength range 3.6 – 500 μm . All imaging and spectroscopy data products will be released to the *Herschel* user generated product archives.

Subject headings: dust, extinction – galaxies: ISM – galaxies: evolution – infrared: galaxies

1. INTRODUCTION

Observations of star formation and the interstellar medium (ISM) in nearby galaxies form a vital bridge between in-depth studies of individual interstellar clouds and star-forming

2100 Copenhagen, Denmark

¹*Herschel* is an ESA space observatory with science instruments provided by European-led Principal Investigator consortia and with important participation from NASA.

regions in the Galaxy and the globally integrated measurements of distant galaxies. Many of the physical processes which are key to triggering and regulating star formation are manifested on kiloparsec or sub-kiloparsec scales. These include the formation and cooling of the atomic gas, the formation of molecular gas and gravitationally bound clouds, the fragmentation of clouds to form bound cores, stars, and star clusters, and the return of radiant and mechanical energy from those stars into the ISM. Until recently this complex interplay of physical processes could only be probed in depth in the Galaxy and close neighbors such as the Magellanic Clouds. The advent of groundbased aperture synthesis arrays at submillimeter to centimeter wavelengths and of sensitive space telescopes in the ultraviolet to submillimeter range have made it possible to extend such work to galaxies in the local Universe, and thus to a range of galactic and interstellar environments which was inaccessible only a few years ago.

These broad aims formed the basis of the *Spitzer* Infrared Nearby Galaxies Survey (SINGS; Kennicutt et al. 2003), one of the six original *Spitzer* Legacy Science projects. The primary goal of SINGS was to fully characterize the infrared emission of galaxies and their principal infrared-emitting components, using imaging of 75 nearby galaxies at 3.6–160 μm along with a suite of spectroscopic mapping of the galaxy centers and selected subregions in the 5–40 μm range. The galaxies and the spectroscopic targets were selected to span broad ranges of physical properties, star formation properties, and local interstellar environments. The *Spitzer* observations of the SINGS sample were supported by an extensive campaign of ancillary observations extending from X-rays to the radio (Kennicutt et al. 2003), and have led to a number of follow-up surveys (many led outside of the original SINGS collaboration), including mapping of the ultraviolet continuum emission (Gil de Paz et al. 2007), radio continuum emission (Braun et al. 2007), velocity-resolved Fabry-Perot mapping of H α emission (Daigle et al. 2006, Dicaire et al. 2008), atomic and molecular gas (Walter et al. 2008; Leroy et al. 2009), and X-ray emission (Jenkins et al. 2011), and optical spectroscopy (Moustakas et al. 2010). As the result of this follow-up work the SINGS sample offers the most comprehensive multi-wavelength dataset for any local galaxy sample of its size ever assembled. Some of the main scientific products of the survey have included comprehensive multi-wavelength spectral energy distribution (SED) atlas (Dale et al. 2007), spectral atlases (Dale et al. 2009; Moustakas et al. 2010); studies of the dust contents and polycyclic aromatic hydrocarbon (PAH) emission (Engelbracht et al. 2006; Draine et al. 2007; Prescott et al. 2007; Smith et al. 2007; Bendo et al. 2008; Muñoz-Mateos et al. 2009a, b) and the molecular gas emission (Roussel et al. 2007); studies of the form and physical origins of the spatially-resolved radio-infrared correlation (Murphy et al. 2006a, b; 2008); testing and calibration of dust-corrected measurements of the star formation rate (e.g., Calzetti et al. 2005, 2007, 2010; Pérez-González et al. 2006; Kennicutt et al. 2009, Li

et al. 2010); studies of the form of the star formation rate (SFR) vs gas density law (e.g., Kennicutt et al. 2007; Bigiel et al. 2008; Leroy et al. 2008; Liu et al. 2011), along with numerous studies of individual galaxies. Most of these investigations exploited the powerful synergies between the infrared observations of the interstellar dust and/or gas emission with coordinated measurements at other wavelengths.

These investigations are now reaching their culmination with the advent of the *Herschel Space Observatory* (Pilbratt et al. 2010). For observations of nearby star-forming galaxies *Herschel's* key capabilities are its spatial resolution for far-infrared (FIR) imaging, its extended wavelength coverage into the submillimeter, and its spectroscopic power for mapping the primary cooling transitions of the gaseous ISM. Although *Spitzer* provided maps of the mid-infrared dust emission (5.8–24 μm) with angular resolutions of 6" or better, its beam sizes at 70 μm and 160 μm , where the bulk of the dust emission is radiated, degrade to $\sim 18''$ and 40" FWHM, respectively, corresponding to typical linear dimensions of 1–5 kpc in the SINGS galaxies. Thanks to a telescope aperture that is four times larger than *Spitzer*, the *Herschel* cameras image the peak of the thermal dust emission with spatial resolutions of a few to several arcseconds, comparable to that of the *Spitzer* 24 μm maps, and sufficient to resolve the emission of dust-emitting clouds from the diffuse disk background emission in most systems.

The spectral region between 50 μm and 250 μm includes some of the primary atomic cooling lines for the neutral and ionized phases of the ISM, including [OI]63 μm , [OIII]88 μm , [NII]122,205 μm , and [CII]158 μm . These lines variously probe the photodissociation regions (PDRs) in the interfaces between molecular, atomic, and ionized gas phases in star-forming regions, the emission of the ionized gas itself in HII regions, and the diffuse atomic gas. When combined with spectral diagnostics from the mid-infrared and visible these lines provide powerful probes of the physical conditions and radiation fields in the ISM, the heating of gas and dust, and potentially robust empirical tracers of star-forming galaxies at high redshift.

These unique scientific capabilities of *Herschel* can only be fully exploited, however, if its imaging and spectroscopy are mated to a comprehensive set of observations at other wavelengths. As such the SINGS project provides an optimal foundational dataset for such a study, and a follow-up *Herschel* survey, KINGFISH (Key Insights on Nearby Galaxies: a Far-Infrared Survey with *Herschel*) was proposed and approved as an Open-Time Key Programme. With 536.6 hours of observing time it is the third largest scientific programme being carried out with the *Herschel Space Observatory*.

The KINGFISH project is an imaging and spectroscopic survey of 61 nearby ($d < 30$ Mpc) galaxies (including 57 galaxies from the SINGS project), chosen to cover the full range of integrated properties and local ISM environments found in the nearby Universe. The

broad goals of KINGFISH are to characterize the ISM of present-day galaxies, the heating and cooling of their gaseous and dust components, and to better understand the physical processes linking star formation to the ISM.

The main aims of this paper are to provide basic information on the core science program, sample selection and properties, observing strategy, data properties and processing, and data products, as a foundation for the numerous science exploitation papers which will follow. The remainder of this paper is organized as follows. In §2 we briefly summarize the scientific objectives for the project and demonstrate how these translated into the experimental design for the *Herschel* observations. In §3 we describe the KINGFISH sample and observing strategy, as well as the *Herschel* observations themselves, and (briefly) the rich set of ancillary data available for the galaxies. This section includes an updated tabulation of the distances and physical properties of the galaxies, so future papers can be consistent in what is assumed. In §4 we describe the processing of the *Herschel* observations and the data products that we plan to deliver from the survey. We also present examples of early KINGFISH observations to illustrate the capabilities of performance of the *Herschel* instruments for this application. Other examples of early KINGFISH observations can be found in the Science Demonstration Phase papers (Beirao et al. 2010, Engelbracht et al. 2010, Sandstrom et al. 2010) and in Walter et al. (2011), Murphy et al. (2011), and Skibba et al. (2011).

2. SCIENTIFIC OBJECTIVES

The KINGFISH science strategy is built around three principal scientific objectives: 1) A comprehensive study of the dust-obscured component of star formation in galaxies, and the relation between star formation and dust heating; 2) A complete inventory of cold dust and its relation to other dust components in the ISM; 3) Spatially resolved studies of the heating and cooling of the ISM, as traced by atomic cooling lines and the dust. The first objective benefits foremost from *Herschel's* excellent imaging resolution, the second from its long-wavelength imaging capabilities, and the third from its unprecedented spectroscopic capabilities. Each of these aims is described in more detail in this section.

2.1. Linking Star Formation to the Interstellar Medium in Galaxies

Approximately half of the bolometric luminosity of the Universe is channeled through the far-infrared (FIR) emission of galaxies (Lagache et al. 2005), and the IR thus carries

information on the full range of heating stellar populations, as well as on the structure and physical conditions of the absorbing dust itself. Dissecting this information in practice is hampered by the highly clumped and variable structure of the stars and dust, and the presence of multiple dust components.

The *Infrared Astronomical Satellite (IRAS)* established some basic global trends in the IR luminosities and colors of galaxies as functions of type and mass, and revealed a separate class of starburst and AGN-driven IR-luminous galaxies (e.g., Soifer et al. 1987). The *Infrared Space Observatory (ISO)* and *Spitzer* Space Telescope missions brought the next breakthrough, by spatially resolving nearby galaxies in the mid-infrared, and by mapping separately the emission of individual dust grain components, each with its own stellar heating population (e.g., Helou et al. 2000; Draine et al. 2007 and references therein; Soifer et al. 2008). These include (1) warm sources associated with gas and dust clouds (HII regions) surrounding young (<10 Myr old) star-forming regions (especially prominent in the *ISO* 15 μ m and *Spitzer* 24 μ m bands); (2) a more diffuse, extended, and cooler dust component heated by stars with a range of ages, which dominates the far-infrared emission (the *IRAS* cirrus component); and (3) mid-infrared band emission from large PAH molecules, transiently heated by single UV and optical photons in PDRs surrounding young star clusters and by the general interstellar radiation field.

These *Spitzer* and *ISO* observations have been especially successful in establishing the physical connections between the heating of the infrared-emitting dust and young stars, but they cannot, because of insufficient angular resolution, separate the various emitting regions and components of most galaxies in the FIR, where the bulk ($\sim 90\%$) of the dust emission occurs. The beam sizes of the *Spitzer* MIPS (Multiband Imaging Photometer for *Spitzer*) imager, for example, are $\sim 18''$ and $40''$ FWHM at 70 μ m and 160 μ m, respectively, corresponding to linear dimensions of 0.9 and 2.0 kpc for a galaxy at a distance of 10 Mpc, similar to the median distance of the galaxies in the SINGS and KINGFISH samples. The larger aperture of *Herschel* allows these wavelengths to be imaged with nearly a fourfold improvement of spatial resolution, with point spread functions of $\sim 5''.5$ and $12''$ FWHM, respectively, at the same wavelengths.

The dramatic improvement in structural information with *Herschel* is illustrated in Figure 1, which compares *Spitzer* MIPS images of the SINGS/KINGFISH galaxy NGC 628 (M74) at 70 and 160 μ m with *Herschel* PACS (Photodetector Array Camera and Spectrometer; Poglitsch et al. 2010) images at the same wavelengths. For galaxies at distances of <30 Mpc (the limit for the SINGS and KINGFISH samples), this difference in resolving power is critical, because it makes it possible to separate star-forming and giant HII regions from quiescent regions, and resolve the nuclear, circumnuclear, and more extended disk emis-

sion. This resolution is also well matched to the physical scales over which cloud formation is triggered, and over which dust reprocesses the light of young stars (e.g., Lawton et al. 2010). The combination of *Herschel* FIR and submillimeter images with the SINGS images at shorter wavelengths provides spatially-resolved SED maps extending from the UV to the FIR.

2.1.1. Understanding and Modelling Dust Heating and Emission in Galaxies

The FIR and submillimeter SED maps from *Herschel* also make it possible to break some of the degeneracies that plague the interpretation of current observations of dust in nearby galaxies. The dust emission and temperature distribution is determined by several factors including the local radiation field intensity, dust opacity, grain size distribution, and composition. *ISO* and *Spitzer* enabled a major advance by providing measurements to treat successfully the heating of the PAH grains and larger FIR-emitting grains separately. The limited wavelength coverage of those data, however, make it difficult to separate the distributions of dust temperatures from the grain emissivity functions.

Herschel's breakthrough capability for this problem is the deep submillimeter imaging capability offered by the SPIRE instrument (Spectral and Photometric Imaging Receiver; Griffin et al. 2010). SPIRE provides confusion-limited images at 250, 350, and 500 μm , sufficient to detect cool dust and constrain the Rayleigh-Jeans region of the main dust emission components. The FIR and submillimeter SEDs can be fitted with dust heating models (e.g., Draine & Li 2007; Draine et al. 2007) to probe dust emission at all ranges of temperatures (from warm dust at $T \sim 100$ K to cooler dust down to $T \sim 15\text{--}20$ K), to test for changes in the wavelength-dependent emissivities with changing metallicity, molecular/atomic gas fractions, and local radiation field environments. These results in turn will constrain the composition and survival properties of the grains, to supplement studies of the Galactic ISM.

The effectiveness of the broad wavelength coverage offered by the combination of *Spitzer* and *Herschel* (PACS + SPIRE) mapping is illustrated in Figure 2, which shows the integrated (full-galaxy) SED of the KINGFISH galaxy NGC 337, with a Draine & Li (2007) dust emission model superimposed.

The spatial resolution of the *Herschel* FIR maps will also make it possible to disentangle the respective roles of different stellar populations in heating the dust. Different age stellar populations have distinct spatial distributions within galaxies, and comparing the surface brightness and color distributions of the IR emission over a wide baseline in wavelengths with those of different stellar populations (readily traced by SINGS UV, broadband visible,

and H α imaging) will allow us to identify the dominant heating populations as a function of location and wavelength, and to constrain the role of other possible sources such as cosmic-ray heating (e.g., Hinz et al. 2004, 2006). The spatially-resolved dust SEDs in galaxies are determined by a combination of factors, including the intensity and spectral shape of the local radiation field, dust opacity, and the heating geometry. Separating these factors requires a sample of galaxies with a wide range of SFRs, distributions of star formation, and dust environments, and the KINGFISH sample was specifically designed to offer this wide range of environments (§3).

The high-angular resolution *Herschel* data will also address another problem raised by *ISO* and *Spitzer* observations, namely the relation of the mid-infrared PAH band emission at 3–18 μm to the other dust components, and the stellar populations which are mainly responsible for powering this emission. *Spitzer* and *ISO* studies revealed at least two important sources of PAH emission in star-forming galaxies: emission from PDRs surrounding star-forming regions, and more extended diffuse PAH emission driven by the general interstellar radiation field, in relative proportions which can vary significantly within and between galaxies (e.g., Helou et al. 2004). Studies have shown that the PAH emission correlates with both the cold ($T \sim 20$ K) dust heated by the general, stellar population (Haas et al. 2002, Bendo et al. 2008) on the one hand, and with the number of ionizing photons from the young stellar population on the other hand (e.g., Roussel et al. 2001, Förster Schreiber et al. 2004). Reconciling these apparently discordant results is handicapped by the limited angular resolution and sensitivity of the available maps of the diffuse cool dust component. *Herschel* now is making it possible to obtain maps of the cool dust component with spatial resolutions that are more comparable to that of the 8 μm PAH band emission, so the stellar populations heating the respective dust components can be compared directly. Understanding the relationships between the PAH emission, large-grain emission, and star formation is also important because the PAHs are believed to be major contributors to the heating of the interstellar gas, especially in PDR regions (§2.3.1).

2.1.2. Robust Multi-Wavelength Star Formation Rates and the Schmidt Law

The detection of large populations of dusty star-forming galaxies at high redshift by *ISO*, *Spitzer*, and now by *Herschel* has underscored the need for reliable calibrations of IR-based and composite UV+IR or visible+IR based SFR diagnostics, and a physical understanding of the basis and limitations of these tools (Kennicutt 1998). The SINGS project has confirmed the close association of the warm 24 μm dust component with the youngest star-forming population in HII regions (Calzetti et al. 2007), which has enabled the derivation of reliable,

extinction-corrected SFR indicators (Calzetti et al. 2007, 2010; Rieke et al. 2009; Kennicutt et al. 2009). However the physical basis and applicability of such calibrations to high-redshift galaxies, which often exhibit vastly higher SFRs and different interstellar environments than found locally, is unclear, because the $24\ \mu\text{m}$ emission comprises typically less than 10% of the total dust emission of galaxies, and the spatial resolution of *Spitzer* at longer wavelengths does not allow for the clean resolution of individual star-forming complexes in most galaxies.

The sub-kpc scale FIR maps provided by the *Herschel* PACS instrument will directly elucidate the relation between the $24\ \mu\text{m}$ emission and the FIR emission at the peak of the bolometric dust emission, in the $70\text{--}170\ \mu\text{m}$ range, for individual star-forming regions. This will make it possible to calibrate directly SFR diagnostics based on composite UV+IR and $\text{H}\alpha$ +IR tracers, for spatially resolved applications within galaxies, and for global studies of more distant galaxies. The same data will quantify the random and systematic errors in SFRs based on IR measurements alone (due to starlight not absorbed by dust). The resulting empirically-calibrated SFR recipes can also be compared to those expected from fitting population synthesis and dust models to the observed SED maps, to test the reliability of these methods in environments that differ substantially from those found in local galaxies (e.g., see Murphy et al. 2011).

The resolved attenuation-corrected *Herschel* SFR maps span a considerably wider dynamic range than is currently available from integrated SFR measurements (e.g., Kennicutt et al. 2009), extending in particular to low surface brightness regimes where $\text{H}\alpha$ no longer necessarily provides a statistically reliable local SFR measure (e.g., Cerviño et al. 2003; Salim et al. 2007. Meurer et al. 2009; Lee et al. 2009). Combining these data with the extensive set of high-angular-resolution HI and CO maps available for this sample (§3.4), enables investigation of the spatially-resolved correlation between the SFR surface density and the gas surface density (Kennicutt 1998b, Kennicutt et al. 2007), variations in the star formation efficiency as functions of local dynamical environment within disks (e.g., Leroy et al. 2008), and the physical nature of the apparent star formation thresholds at low SFR densities in disks (e.g., Martin & Kennicutt 2001).

2.1.3. *The Radio-IR Correlation*

There is a close empirical correlation between the cm-wavelength, synchrotron-dominated emission and the FIR luminosity, which also traces (young) massive star formation (Helou et al. 1985). As a result the radio continuum emission of galaxies is frequently applied as a dust-free tracer of recent star formation, both for local and distant galaxies (e.g., Condon 1992). However, it is entirely unclear how presumably unrelated physical processes affect-

ing the propagation of CR electrons and the heating of dust grains work together to yield a nearly ubiquitous correlation between the radio and FIR emission over many orders of magnitude.

Spitzer revealed that the spatially resolved correlation between $70\ \mu\text{m}$ and non-thermal radio emission within galaxies shows an ‘age effect’: the cosmic ray electron population of galaxies having more intense star formation largely arise from a recent episode of enhanced star formation activity and have not had time to diffuse significant distances (Murphy et al. 2008). This work will be extended with *Herschel* by enabling the study of galaxies over a much larger range of spatial scales and physical parameters than possible so far (Murphy et al. 2011). These comparisons will be carried out using 20 cm maps obtained with the Westerbork Synthesis Radio Telescope (WSRT; Braun et al. 2007), and with new observations obtained with the Expanded Very Large Array, The Australia Telescope Compact Array (ATCA), the Effelsberg 100 m Radio Telescope, and the Robert C. Byrd Green Bank Telescope (GBT). The goal of these studies is to enable the understanding of the underlying physics of radio-IR correlation on scales down to ~ 40 pc.

2.2. The Inventory of Cold Dust in Galaxies

The *ISO* and *Spitzer* observatories made major strides toward compiling a comprehensive inventory of interstellar dust in galaxies. Nevertheless our knowledge has been limited by the relatively few spatially resolved observations of nearby galaxies at wavelengths above $200\ \mu\text{m}$, and by the limited sensitivity of those data. Because of the Planck function and the steep decrease in the opacity of dust at longer wavelengths (approximately as $\lambda^{-\beta}$, with $1 < \beta < 3$ in most cases), cooler dust can radiate relatively little power but still account for most of the mass. As a result the amounts and distributions of colder dust in galaxies ($T < 15$ K) are poorly measured, and systematic uncertainties of factors of two or more in the dust masses of galaxies are not uncommon (e.g., Bendo et al. 2003; Galametz et al. 2011). A combination of *ISO*, *Spitzer*, *Planck*, and ground-based submillimeter measurements of a handful of galaxies show evidence for the existence of extended cold dust, with temperatures as low as 4–6 K (e.g., Hinz et al. 2004, 2006; Meijerink et al. 2005; Galliano et al. 2003; Dumke et al. 2004; Planck Collaboration 2011a, b). On the other hand, analysis of a large sample of SINGS galaxies by Draine et al. (2007) concluded that very cold ($T < 10$ K) dust contributed no more than half of the total dust mass. The FIR and submillimeter maps of galaxies obtained with *Herschel*, when combined with ground-based $850\ \mu\text{m}$ and $1100\ \mu\text{m}$ imaging from LABOCA, MAMBO-2, and SCUBA-2 provide an unprecedented opportunity to map and quantify the cooler dust emission (e.g., Gordon et al. 2010; Meixner et al. 2010). Spatially resolving

the dust emission also will allow us to properly weight the contributions of the different luminosity components (often with very different SEDs) to the integrated emission, and thus constrain any possible biases in deriving dust masses and other parameters.

A related problem revealed by *ISO* and *Spitzer* was the presence of strong submillimetre excesses in the SEDs for some galaxies (e.g., Lisenfeld et al. 2002; Galliano et al. 2003; Israel et al. 2010; Bot et al. 2010; Galametz et al. 2011; Planck Collaboration 2011b). If this excess were associated with a component of very cold dust this material could comprise the dominant dust component by mass in the galaxies, but other possible explanations include emission from (warmer) amorphous dust grains, emission from spinning dust, or free-free radio emission. Previous detections of this submillimeter excess emission in galaxies have been difficult to interpret because the beam sizes of the measurements have often been comparable to the sizes of the entire galaxies. The sensitivity and the sub-kpc spatial resolution of the *Herschel* SPIRE observations, when combined with longer wavelength observations mentioned above, should make it possible to isolate the sources of the submillimeter-excess emission, confirm the physical nature and origins for the emission, and thereby constrain much more accurately the cold dust masses of the galaxies. The multi-wavelength KINGFISH/SINGS maps will also be used to search for extraplanar emission which might be associated with starburst driven winds or galactic fountains.

The *Herschel* submillimeter continuum maps will also shed light on the issue of the constancy of the ratio of CO rotational line brightness to molecular hydrogen surface density, the notorious CO/H₂ X-factor problem (Bollato et al. 2008). Comparisons of the dust surface densities of KINGFISH galaxies to the corresponding column densities of HI and H₂ (the latter derived from CO measurements) provide measurements of the local dust/gas ratio, over ranges of 2–3 orders of magnitude in gas surface density and a factor of 20 or more in metallicity (e.g., Draine et al. 2007). If there are regions in the galaxies where the CO emission severely under-estimates the total molecular gas column, they may be apparent as an anomalously high dust/gas ratio (e.g., Leroy et al. 2007, 2009, 2011). Our tests will make for an excellent comparison to *Fermi* observations which hope to explain the radial gradient in the Galaxy’s diffuse gamma-ray emission. The leading candidate is a radial variation (factor of 5 to 10) in the X-factor (Strong et al. 2004). Using dust to trace H₂ has its own biases and systematics. Because KINGFISH covers a wide range of environments and this method has different biases than dynamical, diffuse gamma ray, or absorption-line approaches it can provide important constraints on the behavior of the CO-to-H₂ conversion factor that complement these other methods.

2.3. The Energy Balance of the Star-Forming ISM

The spectral coverage of the PACS instrument includes several of the most important cooling lines in the atomic and ionized ISM, most notably [CII]157.7 μm , [OI]63.2 μm , [OIII]88.4 μm , [NII]121.9 μm and 205 μm . Even with this limited set of lines the range of astrophysical applications is broad, including mapping of the cooling rates and derived UV radiation intensities in active star-forming regions and the more quiescent ISM, testing and calibrating fine-structure lines such as [CII] 158 μm as a star-formation diagnostic, and constraining the metal abundance scale in HII regions.

2.3.1. Cooling of the Interstellar Medium

The [CII]158 μm and [OI]63 μm far-infrared lines dominate the cooling of the warm, neutral medium in normal galaxies. Photoelectrons liberated from dust grains by UV photons provide the heat input for the gas (e.g., Hollenbach & Tielens 1999). The heating is relatively inefficient (0.1 – 1%), and is determined mainly by the ratio of UV radiation field to density (G_0/n). Observations of the far-infrared cooling lines in representative samples of local star-forming galaxies were pioneered with *ISO* (e.g., Malhotra et al. 1997,2001; Helou et al. 2001; Contursi et al. 2002; Brauher et al. 2008). These studies clearly showed that (1) while the [CII]158 μm emission dominates the line cooling, the ratio of [CII]/FIR decreases by more than an order of magnitude (from 0.004 to less than 0.0004) for galaxies with high luminosity and/or warm dust temperatures, (2) the [OI]63 μm /[CII]158 μm flux ratio ranges from 0.2 – 2, with [OI] taking over as the primary coolant for the high luminosity, warm sources, and (3) the [CII]/PAH ratios show no such trends with dust temperature or luminosity. These results are broadly consistent with a model that explains the ISM having a diffuse or cirrus-like component, where [CII] dominates the cooling and the smallest grains provide the bulk of the heating, together with an “active” component, where [OI]63 μm is stronger than [CII]158 μm .

Near bright star-forming regions, stellar photons from massive (OB) stars are likely to dominate the gas heating. However, shocks, turbulence and cloud-cloud collisions may also contribute in more isolated regions (Flower & Pineau Des Forêts 2010). Unfortunately, the poor spatial resolution of *ISO* and the small numbers of detected sources made comparisons to models extremely difficult (e.g., Kaufman et al. 1999; Contursi et al. 2002). With the addition of *Herschel* KINGFISH observations, the cold dust, PAHs, and the far-infrared cooling lines will be mapped at comparable spatial resolutions, allowing us to trace the heating and cooling of the gas and dust in both active and quiescent regions for the first time in a large sample of nearby galaxies. The KINGFISH sample purposefully includes

galaxies (and subregions of galaxies) with a wide range of star-formation activity, as well as a fraction of galaxies hosting low-luminosity active galactic nuclei (AGNs) AGN (27LINERs from their optical nuclear spectra). This will make it possible to evaluate the impact of non-stellar activity on the dust grain populations (e.g., Smith et al. 2007) and on the cooling of the circumnuclear gas in the presence of X-rays, cosmic rays, and/or large-scale shocks (Meijerink et al. 2007).

2.3.2. *The Range of Physical Conditions of the ISM*

Herschel spectroscopic observations are well suited for revealing the physical conditions and energetics of the neutral ISM in these galaxies. The PACS line observations map the emission of the main [CII] and [OI] cooling lines, as well as the weaker [NII]122 μm , [OIII]88 μm , and (in strong sources) [NII]205 μm lines, with linear resolutions of ≤ 300 pc. This is comparable to the sizes of typical star-forming complexes, and the scales over which the formation of molecular clouds are thought to be triggered. The [NII] and [OIII] lines probe the ionized gas in the obscured, star forming complexes and allow for an estimate of the gas density and the effective temperature of the ionizing stars. The [NII]122/[NII]205 line flux ratio is a sensitive probe of gas density, for densities of $10 < n_e < 1000 \text{ cm}^{-3}$, lower than that probed with the mid-infrared [SIII] lines seen with *Spitzer*. The combination of spectral line information from *Herschel* and SINGS mid-infrared spectra in the 10–40 μm region with *Spitzer* will provide critical measurements of the physical conditions in the ISM— temperatures, densities and pressures, local UV radiation strength and hardness, and constraints on the clumping of the gas on scales much smaller than the beam resolutions.

As with nearly all of the investigations being carried out in KINGFISH most of the diagnostic power of the spectroscopy is exploited in combination with the matching *Spitzer* observations, in this case with the mid-infrared spectroscopy. As an illustration of this synergy, Figure 3 plots each of the detectable transitions in terms of ionization potential and critical density.

2.3.3. *Tracing Star Formation with Cooling Lines*

Understanding how to use the [CII]158 μm (and other FIR fine structure lines) to estimate the SFR in galaxies is timely and important. These features are already being observed in some luminous star-forming galaxies at high-redshift, with a variety of instruments on the ground and in space. The ability to detect the [CII] line (as well as [OI] and [OIII]) out

to extremely high redshifts and measure the SFR in extremely young galaxies is a key science driver for the Atacama Large Millimeter Array (ALMA). This capability has recently been highlighted by the kpc-scale image of the redshifted [CII] line in the $z = 6$ QSO SDSS J114816.6+52 obtained with the IRAM Plateau de Bure millimeter interferometer (Walter et al. 2009). This object has an implied SFR of nearly $2000 M_{\odot} \text{ yr}^{-1}$. Similarly, detection of the [CII] line in the $z = 1.3$ ULIRG MIPS J142824.0+352619 (Hailey-Dunsheath et al. 2010) and in a dozen more galaxies at $1 < z < 2$ (Stacey et al. 2010) have provided evidence for massive, galaxy-wide starbursts at early epochs.

Before these cooling lines are applied indiscriminantly as SFR tracers, it is important to test their accuracy and reliability using nearby galaxies where the SFR can be accurately measured using other methods. Observations of M31 by Rodriguez-Fernandez, Brouillet, and Combes (2006) show that the [CII] emission follows both the $H\alpha$ and *Spitzer* MIPS $24\mu\text{m}$ emission, suggesting its use as a star-formation diagnostic, at least on small scales. A calibration of the [CII] line as a global SFR tracer was derived by Boselli et al. (2002). Their calibration was limited to normal late-type galaxies, but even then the derived SFRs had uncertainties of roughly a factor of ten. Comparisons of the integrated [CII] and FIR luminosities of a more diverse sample of galaxies (e.g., Malhotra et al. 1997; Gracia-Carpio et al. 2011) show that this correlation sometimes breaks down even more severely, particularly in the regime where [CII] no longer dominates the cooling, or when starlight from evolved populations dominates the grain photoelectric heating. By mapping the key FIR cooling lines in the KINGFISH sample we will not only shed light on the range of physical conditions within normal galaxies, but we will also establish a critical local baseline against which to compare the observations of high-redshift galaxies in the coming decade.

2.3.4. *Metal Abundances and the Nebular Abundance Scale*

The KINGFISH spectroscopy includes measurements of the [OIII] $88\mu\text{m}$ line, a powerful cooling line for HII regions around early-type O stars. Combining the KINGFISH maps in this line with matched-aperture optical spectra from SINGS and the literature will help resolve the longstanding discrepancy between the HII region metal abundance scale as calibrated by conventional optical spectroscopy based on auroral-line electron temperatures, *vs* those derived from HII region models fitted to strong lines, *vs* those measured from optical recombination lines (e.g., emission lines of OII that are produced by recombination from OIII). Discrepancies of up to factors of 2–3 between these calibrations remain present today (e.g., Kennicutt et al. 2003; Perez-Montero & Diaz 2005; Kewley & Ellison 2008). Various explanations for the discrepancies have been offered, including the possible presence of

temperature fluctuations which would bias the auroral line measurements; however recent comparisons of nebular and stellar temperature scales appear to point more in the direction of systematic errors in the model-derived abundance scales (Bresolin et al. 2009). The [OIII] $88\mu\text{m}$ line, which arises from the ground level of the optical [OIII] 4959,5007 transitions, provides an independent measurement of the O^{++} abundance that is much less sensitive to temperature fluctuations (e.g., Rudolph et al. 2006). Calibration of the density dependence of the emission is provided by the SINGS spectroscopy of the [SIII] $18.7\mu\text{m}$ and [SIII] $33.5\mu\text{m}$ lines, an excellent example of the power of combining *Spitzer* and *Herschel* spectroscopy.

3. OBSERVATIONS

3.1. The KINGFISH Galaxy Sample

The scientific potential of KINGFISH derives from combining the power of deep infrared imaging with spectroscopy of the key diagnostic lines, and the vast ancillary data heritage of SINGS. To maximize the benefits the KINGFISH imaging and spectroscopy have been closely tailored to the existing SINGS observations.

The SINGS sample comprises 75 galaxies within 30 Mpc, selected to cover the range of galaxy types, the range of galaxy luminosities and masses within each type, and the range of dust opacities (as traced by the ratio of IR to visible luminosities) within this type-mass space with a strong bias toward star-forming galaxies (see Kennicutt 2003 for details).

The KINGFISH survey did not need to include all 75 galaxies in the SINGS sample. Ten galaxies had already been allocated extensive observing time as parts of *Herschel* Guaranteed Time programs. Careful examination of the multi-wavelength data available the 65 remaining galaxies allowed us to reduce the KINGFISH sample by a further eight galaxies. The galaxies excluded (NGC 24, 1566, 4450, 4452, 5033, IC 4710, Ho IX, M81dwA) have physical properties and infrared emission properties which were very similar to other galaxies in the sample. At the same time we added four other nearby galaxies which were drawn from *Spitzer* surveys other than SINGS, and which augmented significantly to the range of physical properties covered by the KINGFISH sample. M101 (NGC 5457) is one of the largest spirals in the local volume and exhibits one of the largest metal abundance gradients with galactocentric distance found in a nearby disk galaxy. IC 342 is one of the nearest giant spiral galaxies and exhibits an unusually large contrast in star formation properties between a dense starburst nucleus and a very extended disk. NGC 3077 is a peculiar, starburst galaxy in the M81 group, that helps complete our coverage of that group. Finally NGC 2146 is an unusually dusty early-type galaxy, one of the nearest LIRGs, and the most IR-luminous

galaxy in the sample.

The properties of the KINGFISH galaxies are summarized in Table 1. The values tabulated are much improved thanks to new observations from SINGS and elsewhere, and supercede those published earlier by Kennicutt et al. (2003). Recession velocities, morphology, and projected sizes are from NED, the NASA Extragalactic Database². Sources for the other data are given in the extensive set of table notes, and are summarized below.

Column (1): Galaxy identification

Column (2): Heliocentric radial velocity, from NED

Column (3): Morphological type, from NED

Column (4): Approximate major and minor diameters in arcminutes, as listed in NED. These are approximately consistent with RC3 D_{25} diameters (de Vaucouleurs et al. 1991).

Column (5): Adopted distance in megaparsecs.

Column (6): Method used for adopted distance. The distance for each galaxy was based on a redshift-independent indicator, using, in order of preferences: Cepheid variable stars (Ceph), tip of the red giant branch stars (TRGB), surface brightness fluctuations (SBF), Type 2 plateau supernovae (SNII), Tully-Fisher relation (TF), and brightest stars (BS). For M81DwB we used the mean distance of the M81 Group (M81G — 3.6 Mpc), as no other distance measurement is available for this galaxy.

Column (7): Reference for distance measurements, as documented in the table notes. The source of the references is the compilation contained in NED, and we have attempted to draw the distances from the largest compilations we could find, in order to minimize the number of different sources and reduce inconsistencies among different distance measurements.

Column (8): Nuclear type, when available, as derived from optical emission line diagnostic plots constructed from nuclear spectra. These classifications come from Moustakas et al. (2010) or (denoted by asterisks) Ho, Filippenko & Sargent (1997). The abbreviation SF denotes an HII region-like spectrum, and AGN an accretion disk spectrum (LINER or Seyfert). Readers should note that although a considerable number of KINGFISH galaxies show non-stellar nuclear emission most of these are low-luminosity AGNs. With the exception of NGC 1316 = Fornax A none of the galaxies hosts a dominant AGN. Galaxies without

²The NASA/IPAC Extragalactic Database (NED) is operated by the Jet Propulsion Laboratory, California Institute of Technology, under contract with the National Aeronautics and Space Administration.

a listed nuclear type either lack nuclear emission lines, have completely obscured nuclei in the visible (e.g., NGC 1377), or in the case of most of the dwarf galaxies lack discernable nuclei altogether.

Columns (9) and (10): Mean disk logarithmic oxygen abundance. We have adopted the disk-averaged oxygen abundances ($12 + \log O/H$) from Table 9 of Moustakas et al. (2010). These authors list two values for each galaxy: one from the theoretical calibration of Kobulnicky & Kewley (2004; denoted KK) and the other from the empirical calibration of Pilyugin & Thuan (2005; denoted PT). Both sets of measurements are listed in the table. We refer the reader to Moustakas et al. (2010) and the papers cited in §2.3.4 for a full discussion of the bases and uncertainties inherent in the two abundance calibrations. For galaxies lacking HII region measurements the oxygen abundances are estimated from the luminosity-metallicity relation (as denoted by + symbols). For the four galaxies that were not originally in the SINGS sample (IC 342, NGC 2146, NGC 3077, and NGC 5457), we have used values from the literature: (B) Bresolin et al. (2004); (C) Calzetti et al. (2004); (E) Engelbracht et al. (2008); (P) Pilyugin et al. (2004).

Column (11): Luminosity at $3.6 \mu\text{m}$ (a proxy for stellar mass), as derived from flux densities published in Dale et al. (2007, 2009) and Engelbracht et al. (2008) and the distances listed in Column (5).

Column (12): Total infrared luminosity in the range $3\text{--}1100 \mu\text{m}$, L_{TIR} , are derived from the flux densities at 24 , 70 , and $160 \mu\text{m}$ listed in Dale et al. (2007, 2009) and Engelbracht et al. (2008) and the distances listed in Column (5). Equation (4) of Dale & Helou (2002) was used to derive L_{TIR} from the fluxes at 24 , 70 , and $160 \mu\text{m}$.

Column (13): Star formation rate, in units of $M_{\odot} \text{ yr}^{-1}$, derived using the combination of $H\alpha$ and $24 \mu\text{m}$ emission as calibrated in Kennicutt et al. (2009), and tabulated in Calzetti et al. (2010), adjusted to the distances Column (5). For NGC 5457, the $H\alpha$ luminosity is from Kennicutt et al. (2008) and the $24 \mu\text{m}$ luminosity from Dale et al. (2009).

Column (14): Total stellar mass in units of solar masses, derived using the method of Zibetti et al. (2009), and published by Skibba et al. (2011), but rescaled when necessary to the distances adopted here.

Column (15): Classification of the galaxy as a high surface brightness (B) or faint surface brightness (F) system for the PACS and SPIRE observations, as described in §3.2.

Figure 4 illustrates the distribution of galaxy types and SFRs of the galaxies in the KINGFISH sample, plotted in both cases as functions of distance, to give a sense of the linear resolution available for specific classes of galaxies. As expected, the distribution of

morphological types is fairly independent of distance, except for the irregular galaxies, which are overwhelmingly clustered in the lowest distance bin on account of being mostly faint galaxies (Table 1). There is also a weak trend for earlier type galaxies to populate larger distance bins, on account of these types usually being larger, more luminous galaxies. Similarly, low SFRs are generally found in the lowest distance bins. Most of the closest low-SFR galaxies are gas-rich dwarfs. Unusual types of galaxies, for example early-type galaxies with high SFRs, tend to lie at larger distances, because they are rare objects and only appear when one probes a larger cosmic volume.

In terms of other properties the KINGFISH sample covers nearly two orders of magnitude in oxygen abundance ($7.3 < 12 + \log(O/H) < 9.3$, four orders of magnitude in $3.6 \mu\text{m}$ luminosity ($\sim 10^6\text{--}10^{10} L_{\odot}$), and in total infrared luminosity ($\sim 4 \times 10^6\text{--}10^{11} L_{\odot}$), and a similar total range in SFRs ($\sim 0.001\text{--}7 M_{\odot} \text{ yr}^{-1}$).

Figure 5 shows the distribution of the KINGFISH galaxies in terms of the well known bimodal relation between specific SFR (SSFR) and stellar mass. Most of the galaxies populate the star-forming “blue cloud”, which reflects the deliberate survey bias to actively star-forming systems. However higher-mass galaxies with low SFRs consistent with the red sequence are also represented in the sample, though they tend to be early-type spirals rather than E–S0 systems. The sample lacks examples of the most massive red galaxies. Also apparent is the lack of clear separation in SSFRs between early-type and late-type galaxies. This again reflects the design of the SINGS and KINGFISH samples; we deliberately included galaxies with a wide range of infrared luminosities independent of morphological type, so the sample contains unusually large numbers (relative to any volume-limited sample) of peculiar early-type galaxies, often with relatively high infrared luminosities and SFRs.

3.2. PACS and SPIRE Imaging

A subsample of 55 galaxies are being imaged with PACS+SPIRE to well beyond the optical radius at 70, 100, 160, 250, 350, and $500 \mu\text{m}$; the remaining 6 KINGFISH galaxies, which are also part of the *Herschel* Reference Survey Guaranteed Time Key Project (Boselli et al. 2010a), are imaged with PACS alone. Our map sizes are designed to probe cool dust, if present, outside the optical disk and to provide sufficient sky coverage to remove instrumental artefacts; we thus acquire for all galaxies with both instruments square maps of dimension at least 1.5 times the optical diameter. A minimum map size of 10×10 arcmin is imposed in order to maximize efficiency, given the observing overheads, and better standardize observations. At the SPIRE wavelengths, sensitivity is limited by confusion even for modest exposure times. On the other hand, at the shortest PACS wavelengths we cannot

easily reach the confusion limit, so we chose instead to obtain sufficient depth to detect the diffuse disk emission within 80-90% of R_{25} , and to detect individual IR sources with high signal/noise beyond R_{25} . The goal is to map the diffuse emission at PACS fainter surface brightness levels through a strategy of smoothing and combination with the SINGS 70 and $160\ \mu\text{m}$ MIPS images, which are much deeper on large angular scales.

The *Spitzer* MIPS images for these galaxies show that the sample spans a wide range in FIR surface brightnesses at the optical radius R_{25} (Munoz-Mateos et al. 2009). We therefore evaluated the $160\ \mu\text{m}$ surface brightness $\Sigma_{160\mu\text{m}}$ at R_{25} , and analyzed the histogram of the resulting $\Sigma_{160\mu\text{m}}$ values. This enabled us to divide the sample into two groups, a “bright” (high FIR surface brightness at R_{25}) group with median $\Sigma_{160\mu\text{m}} \sim 3\ \text{MJy sr}^{-1}$ and a “faint” one (low surface brightness) with $\Sigma_{160\mu\text{m}} \lesssim 1\ \text{MJy sr}^{-1}$. These two subsets are listed as B and F, respectively, in Column (15) of Table 1. Our observations were devised to achieve these 1σ per-pixel sensitivities at R_{25} at $160\ \mu\text{m}$. By adjusting the exposure times between the two groups we were able to optimize the requested time allocation.

The SEDs of most of the KINGFISH galaxies peak in the $75\text{--}170\ \mu\text{m}$ region and fall off rapidly at longer wavelengths (Figure 2). Since the primary goal of our imaging is to accurately map the distributions of dust mass and temperature, we need to tailor our exposure times to provide comparable signal/noise for a typical galaxy SED across this wide range in wavelength. For most of the galaxies, this required an estimated extrapolation of the brightness distributions into the submillimeter. This was done using the MIPS $\Sigma_{160\mu\text{m}}$ at R_{25} together with empirical or model SED estimates (Dale et al. 2007).

To maximize efficiency, we have adjusted our exposure times to achieve comparable sensitivity across the range in wavelengths spanned by PACS+SPIRE, and better constrain the distributions of dust mass and temperature in the outer regions of the galaxies. The PACS maps are acquired in scan mode at medium speed of $20''\ \text{s}^{-1}$, with homogeneous coverage and the array oriented at a 45° angle relative to the scan direction. Each PACS blue wavelength observation ($70\ \mu\text{m}$ and $100\ \mu\text{m}$) consists of two chained AORs, with perpendicular scans to minimize detector anomalies. Four AORs per galaxy are required for complete PACS coverage, since PACS acquires a single blue wavelength simultaneously with the red one ($160\ \mu\text{m}$). Hence an observation consisted of two observations at $70\ \mu\text{m}$ and $100\ \mu\text{m}$ and four at $160\ \mu\text{m}$. These procedures were also adopted to filter out transient phenomena (e.g., asteroids). Each AOR consisted of three scan repetitions for bright targets and six repetitions for faint targets.

The SPIRE observations were performed similarly, using the Large Map mode at the nominal scan speed of $30''\ \text{s}^{-1}$, with the array oriented in two orthogonal scans at 42.4° and -42.4° relative to the scan direction. Galaxies were observed in a single AOR with two and

four repetitions for the bright and faint group, respectively. Table 2 lists pixel sizes and approximate sensitivity limits for each wavelength in the PACS and SPIRE observations. Note that at the longest wavelengths the observations are confusion limited (Nguyen et al. 2010).

For IC 342, the largest galaxy in our sample, we used the Parallel Mode, in which PACS and SPIRE observations are acquired simultaneously. Again, we required complete PACS coverage, so we used two repetitions at slow speed ($20'' \text{ s}^{-1}$) in orthogonal directions for each PACS blue wavelength, in order to better remove striping, $1/f$ noise, and mitigate beam smearing along the scan direction. Estimated sensitivities are given in Table 2.

3.3. Spectroscopic Observing Strategy

The KINGFISH spectroscopic observations consist of spectral mapping in the key diagnostic emission lines [CII] $158\mu\text{m}$, [OI] $63\mu\text{m}$, [OIII] $88\mu\text{m}$, [NII] $122\mu\text{m}$, and (in areas of high surface brightness) [NII] $205\mu\text{m}$. The observing strategy closely follows that of the SINGS project, covering nuclei, selected extra-nuclear regions, and full radial strips out to a limiting surface brightness threshold. All of the targeted regions have been mapped previously with the *Spitzer* IRS spectrometer. The galactic centers and extra-nuclear regions were observed at low resolution with *Spitzer* from 5–14 μm , and with the *Spitzer* high-resolution spectrometer at 10–37 μm . The radial strips coincide with low-resolution SINGS radial strip maps covering 14–38 μm .

Utilizing the $47'' \times 47''$ PACS spectrometer field of view, a total of 51 nuclear pointings, 28 strips (covering 115 PACS fields of view), and 41 extra-nuclear positions in 14 separate galaxies were targeted. The selection criteria for the extranuclear regions was a physically-based strategy to ensure the widest possible coverage in metal abundance, infrared surface brightness, and $8/24\mu\text{m}$ flux ratios (high $24/8$ values are indicative of dust heated by the intense radiation fields associated with star-forming regions; e.g., Draine & Li 2007). A small number of SINGS targets were dropped entirely from the KINGFISH spectroscopic sample due to non-detection in *Spitzer* MIPS wavebands. An example of the PACS + *Spitzer* spectroscopic targeting is given in Figure 6.

Line surface brightness projections were based on nominal scalings from the total infrared (TIR) surface brightness derived from the SINGS MIPS photometry, together with average fractional line luminosity measurements of nearby galaxies from the *ISO* Key Project (Malhotra et al. 2001). Observations of strips were truncated when the peak projected TIR surface brightness within a single pointing of PACS fell below $10^{-7} \text{ W m}^{-2} \text{ sr}^{-1}$, with ad-

ditional slight trimming to adjust for time constraints and requirements on the cadence of background observations. Targeted regions (strips, single nuclear pointings, and extra-nuclear regions) were divided into three bins of total infrared surface brightness, and line repetitions were chosen to deliver signal-to-noise of at least 5 for the median brightness within each bin. A minimum of one repetition per raster position was allocated for [CII] in the brightest bin, with a maximum of 4 repetitions for [OI] and [NII] in the faintest bin. Where possible, multiple line observations of a given target were grouped into a single AOR. The sensitivity of these maps varies with wavelength (due to changes in sensitivity across the spectral range), but for areas with full depth coverage a typical $1\text{-}\sigma$ sensitivity is $2 - 4 \times 10^{-9}$ W m^{-1} sr. This noise is measured from single-pixel extractions ($2''.85$ pixels). Lower surface brightness sensitivities can be achieved by averaging over larger regions before fitting the spectra.

Since a substantial majority of the sample is comprised of galaxies with photometric radius larger than the maximum PACS chopper throw angle, *unchopped* line scan mode was used. In early tests on two smaller KINGFISH galaxies for which additional chopping observations were obtained, line fluxes and sensitivity per unit observing time compared favorably (within the calibration uncertainty limits) between maps created with and without chopping. In individual targeted regions, a 2×2 sub-pixel dither pattern of $4''.5 \times 4''.5$, or 0.48×0.48 PACS spectrometer pixels, was utilized to mitigate the undersampling of the beam delivered by the telescope, which is particularly significant at the shortest wavelengths.

For the full radial strips, a dither pattern of $23''.5 \times 4''.5$ was used, both to help recover the undersampled beam and minimize coverage gaps at the perimeter of the maps. This effectively increases the observing time per pixel in most areas by a factor of four over that of a single raster position. Since the radial strip position angles were dictated by preexisting *Spitzer* IRS observations, no attempt was made to adapt the roll angle of the square PACS spectrometer field to this angle. In practice this leads to little or no loss of joint coverage between the *Spitzer* IRS long-low scan maps and the corresponding PACS maps.

Offset background fields were specified nearby in areas of low infrared surface brightness, and were visited at least every 2 hours, which, in the case of galaxies with long radial strips, required multiple background visits during individual line scans.

3.4. Ancillary Multi-Wavelength Observations

Achieving the main scientific aims of this project requires a strong set of multiwavelength data extending from the UV to the radio to complement the *Herschel* observations. These

provide essential information on the gas and dust emission at shorter wavelengths than probed by *Herschel*, the stellar populations which heat the dust and ionize the gas, and the associated cold and warm gas components.

Most of these ancillary datasets were assembled for the SINGS project (Kennicutt et al. 2003), or were carried out by other groups in parallel with the SINGS project. Briefly the imaging data include ultraviolet images (153 nm and 230 nm) from *GALEX* (Gil de Paz et al. 2007), ground-based B,V,R,I, and H α images, Fabry-Perot H α maps and velocity fields (Daigle et al. 2006, Dicaire et al. 2008), near-IR J, H, and K imaging compiled from the 2MASS survey (Jarrett et al. 2003), and of course the *Spitzer* imaging at 3.6, 4.5, 5.8, and 8 μ m (IRAC) and at 24, 70, and 160 μ m (MIPS). Radio continuum maps are available from the WSRT (Braun et al. 2007) and the VLA, and Chandra X-ray imaging for approximately 75% of the sample is being obtained or compiled (Jenkins et al. 2011).

Deeper visible and near-infrared broadband imaging of the northern KINGFISH sample is being obtained in the *g*, *I*, and *H*, using the wide-field imagers at the Calar Alto Observatory. These are explicitly designed to be able to produce high-quality stellar mass maps of the galaxies based on state of the art stellar populations models (Zibetti et al. 2009).

A number of the galaxies in the KINGFISH sample are near enough to have deep HST imaging of the resolved stellar populations, for example through the ACS Nearby Galaxy Survey Treasury (ANGST; Dalcanton et al. 2009). Those observations can be used to derive spatially-resolved star formation histories (e.g., McQuinn et al. 2010a, b; Weisz et al. 2011), and strong independent constraints on SFRs and star formation timescales derived from integrated light.

Spectroscopy includes ground-based optical spectra (3,700–7,000Å; Moustakas et al. 2010), *Spitzer* IRS (low and high resolution, 5–40 μ m) and MIPS SED (50–100 μ m) spectral maps. The SINGS IRS spectral maps (low-resolution spectral strips, circumnuclear maps, extranuclear region maps) are an especially unique resource. *Spitzer* spectra are obtained with fixed slits, and one needs multiple-pointing maps to properly interpret the combined spectra, especially in nearby galaxies where sources are extended and often multiple sources are blended in the beam at the longest wavelengths.

A number of radio line surveys have targeted subsets of the SINGS and KINGFISH samples, to study the relationships between the cold gas, dust, and star formation in the galaxies. THINGS (Walter et al. 2008) produced atomic gas (HI) maps of 24 KINGFISH galaxies with $\sim 6''$ resolution. For another 21 galaxies, we have somewhat lower quality ($\sim 15''$ resolution) HI imaging from new or archival VLA and WSRT observations. Thus a total of 45 KINGFISH targets have in-hand atomic gas maps with the exceptions being

southern and early-type galaxies. The HERACLES survey (Leroy et al. 2009) used the IRAM 30-m telescope to obtain deep, wide-field CO $J = 2 - 1$ maps of 41 KINGFISH targets. Other CO $J = 1 - 0$ surveys are being carried out with the CARMA array and the Nobeyama Radio Observatory, and CO $J = 3 - 2$ observations of the centers of many of the galaxies are being obtained at the JCMT as part of the JCMT Nearby Galaxies Legacy Survey. Likewise radio continuum observations of the galaxies or regions within the galaxies are being carried out on a number of facilities, as discussed already in §2.1.3 (also see Murphy et al. 2011). Although the teams on these projects often include members of the KINGFISH collaboration most are independent undertakings, and the corresponding datasets will be produced and released independently from the KINGFISH project.

4. Data Processing, Analysis, and Data Products

As appropriate for a large Key Programme the *Herschel* observations from KINGFISH will be converted to fully documented data products for archival use by the community. In this section we briefly describe the processing and expected nature of the public data products.

Most of the data processing is performed within the *Herschel* Interactive Processing Environment (HIPE; Ott 2010), with subsequent customized processing as described below. The KINGFISH observations present particular challenges in the data processing, with significant emission over a wide range of spatial scales, and (for spectroscopy) with target sizes that are large compared to the standard chopping throw of the PACS spectrometer. At the time of submission of this paper the higher-level processing was still under development. Here we describe the basic principles and objectives of the data reduction efforts; more detailed documentation will be provided as part of the future KINGFISH data releases.

4.1. PACS Scan Maps

At the wavelengths covered by PACS the KINGFISH galaxies are expected to emit fluxes on a range of spatial scales, ranging from unresolved point sources to diffuse emission on scales extending to at least an order of magnitude larger than the instrumental PSF. The presence of this extended structure in the presence of observations with a high thermal background poses a challenge for the processing of the PACS observations. Early tests by our group and others reveal that the recovery of diffuse emission is strongly dependent on the processing algorithms used. As a result we are applying more than one approach to

the PACS data processing. We first describe a standard reduction using a slightly modified version of the HIPE algorithms, and then describe a separate reduction which combines low-level HIPE processing with a separate mapping stage using the Scanamorphos package (Roussel 2011).

4.1.1. Initial HIPE Processing

The PACS processing mostly follows the recommended standard procedure (i.e. pointing association, conversion from engineering units to physical units, flat-fielding). This provides pixel timelines that are almost ready to be reprojected in the sky to produce a map. Prior to this operation, however, one needs to correct the recorded signals for cosmic ray events and $1/f$ noise (the latter corrected in the post-Level 1 processing described here). Anomalies (glitches) are removed using the so-called second-level deglitching method. Instead of inspecting bolometer timelines for outliers, each individual readout is compared to the estimated sky value at the same sky position to identify outlier values. This reference is composed of readouts from different pixels in the detector, thus it is necessary to first remove the relative pixel-to-pixel offsets. This is achieved either by subtracting a median image, or by applying a high-pass filter with a very large filtering window. This method has proven to be more robust than the default pipeline method, in particular with respect to avoiding rejection of compact sources which can mimic instrumental artifacts in their timeline signature. Another advantage of the second-level deglitching is that it also flags pixels that are severely affected by cross-talk effects, as those are obviously outliers with respect to the sky value at their pointing position.

Once the data have been deglitched, flat-fielded, and calibrated into physical units, maps are generated using two different approaches as described below.

4.1.2. PhotProject maps

Low-frequency noise is the dominant source of uncertainty in the PACS images of extended sources. Unlike SPIRE, the PACS photometer does not sample the temperature of its focal plane with sufficient accuracy to enable the removal of thermal drifts from the data. Therefore a strategy using only the signal must be used to separate the $1/f$ noise from the signal of interest. This requires the application of a median high-pass filter to the data before reprojecting the time series scans back to the sky. Smaller filtering windows would better sample the time variation of the thermal drifts, but small filter windows also risk removing

more of the real extended emission from the source. Therefore this filtering is only applied to the section of the scans which do not cover the target. We determine the location of the target in the timeline by projecting a mask, made on a first rough version of the map, into the timelines using the pointing information. Once this is done, the map is created with the `PhotProject` task of HIPE that implements the drizzle algorithm.

Some maps can present a striped pattern appearing in small patches over the field. This is due to electrical interferences that are picked up by the readout circuits. The very low-level of these interferences make them very difficult to detect and remove, and at this time there is no efficient method available for eliminating these artifacts entirely.

4.1.3. *Scanamorphos maps*

Currently the preferred processing of the KINGFISH PACS observations is carried out using the Scanamorphos software³ (Roussel 2011). Its main task is to subtract the brightness drifts caused by the low-frequency noise (comprising both the thermal drifts of the telescope and detectors and the uncorrelated 1/f noise of the individual bolometers), before projecting the data onto a changeable spatial grid. The algorithm employs minimal assumptions about the noise and the signal, and extracts the drifts from the data themselves, taking advantage of the redundancy built in the scan observations. With the nominal settings used by the KINGFISH survey, the drifts can be determined on timescales greater than or equal to 0.7 s at 70 and 100 μm , and 0.9 s at 160 μm (for a sampling interval of 0.1 s). These timescales correspond to lengths between 1.5 and 2.5 times the beam FWHM, from 160 μm to 70 μm . The second-level deglitching was performed, and the option to detect and mask brightness discontinuities was also used. The data are weighted by the inverse square high-frequency noise of each bolometer in each scan.

The output of Scanamorphos is in the form of a FITS data cube for each band. The four planes of the data cube are a signal map, error map, a map of the drifts that have been subtracted, and the weight map. Currently there is no propagation of errors associated with the successive processing steps in the pipeline. For each pixel, the error is defined as the unbiased statistical estimate of the error on the mean. The brightness unit is Jy/pixel, and the pixel size is one fourth of the beam, as listed in Table 2.

Over the past year our team has invested considerable effort into quantifying the uncertainties introduced both into integrated photometry and spatially-resolved mapping of the

³<http://www2.iap.fr/users/roussel/herschel/>

FIR emission in the PACS maps. These include intercomparisons of PACS maps produced with different processing algorithms and independent comparisons with maps produced by *Spitzer* MIPS, *IRAS*, and other instruments. Based on our preliminary comparisons it appears that the Scanamorphos processing preserves most of the extended emission in most of the galaxies analyzed to date, and we plan to deliver these as our primary PACS data products during at least the early stages of the project. More documentation on the processing and uncertainties in the maps will be provided as parts of those future deliveries.

4.2. SPIRE Scan Maps

The raw KINGFISH SPIRE data are processed through the early stages of HIPE to apply all of the standard corrections to Level 1 (including deglitching), and to convert the data to physical units of flux density. A line is fit to the data for each scan leg after masking out the galaxy, and this fit is subtracted from the data. Discrepant data (usually a rogue bolometer, of which there are typically fewer than one per map) are also masked, and the data are mosaicked using the naive mapper in HIPE. The map coordinates are then adjusted so that the positions of the point sources (measured using StarFinder; Diolaiti et al. 2000) match the positions in the MIPS 24 μm images (with an average correction of $\sim 3''$). Finally, the images are converted to surface brightness units by dividing by the beam areas published in the SPIRE Observer’s Manual: 426, 771, and 1626 sq arcsec at 250, 350, and 500 μm , respectively. The output of our pipeline is six simple FITS files for each galaxy, comprised of a calibrated image and uncertainty map for each of the three bands.

4.3. PACS Line Maps and Data Cubes

Readout sample ramps of raw PACS spectral data are fitted onboard the *Herschel Space Observatory*. The fitted ramps are then calibrated and processed using HIPE. After basic calibration and the insertion of instrument status information into the meta-data associated with an observation, data samples are separated based upon the observed grating positions. Each observed line is processed independently from other lines observed during the same AOR. Because motions of the telescope can affect the baseline level of a pixel, individual raster positions are treated independently. When data lack chopping offset fields a canonical dark image is subtracted from each pointing.

The reliability of unchopped mode observations is significantly enhanced by the large amount of redundancy in the data. During each repetition of an unchopped line scan, each

spectral pixel at a given spatial position samples precisely the same wavelength 20 times (in two sets of up-down grating scans of 75 steps per scan, with 5 readouts per grating step). The 16 individual spectral pixels at each spatial position together sweep out a slightly larger wavelength range, and further increase the density of wavelength sampling. Additional repetitions add to this redundancy. This large series of repeated scans is referred to as a “data cloud”.

Pixel-to-pixel baseline response variations are found to be several times larger than the predicted continuum levels underlying each line. Therefore, readout sequences are normalized by subtracting a low-order polynomial fit to the time sequence of data for each pixel, omitting those readings which sample the line itself. All data at a given spatial position are then binned within a wavelength grid that oversamples the theoretical resolution by a factor of two. Each wavelength interval in the final binning has ~ 100 individual samples contributing (per repetition). Within each bin, data that deviate from the bin mean by more than three standard deviations are flagged as outliers and rejected.

Carefully positioned off-source fields, which are free of known infrared sources, are observed with a cadence of at least one every two hours, using one repetition of the same line scanning sequence. Data from these positions are combined to create a generalized background spectrum. The background spectrum at each spatial position is fitted with a low order polynomial to create a noise-free background map, which is then subtracted from each raster position in an observation. Background-subtracted data are produced for each raster position individually.

Final data cubes for each galaxy are obtained by projecting all raster positions of a given line onto a common set of coordinates based on *Herschel* pointing information recorded in the meta data. Pointing uncertainty is of order $3''$. At the $\sim 10''$ resolution delivered, this pointing uncertainty does not significantly degrade the image quality.

Spectral line maps are obtained for each galaxy by applying a multi-step fitting procedure on the data cube. Gaussian fits are performed on each spectrum of the cube, after removing a third order baseline excluding the spectral line region determined by the neutral hydrogen systemic velocity and velocity range information. This process yields peak surface brightness, integrated intensity, velocity centroid, and line-width for each pixel of the cube.

In those pixels where the fit fails to meet a number of validity criteria (for example, the centroid found is outside the allowed HI velocity range) the fit is replaced by straight integration. Spectra are integrated on a range of velocities corresponding to the [CII] emission at that position, or based on the HI information if the [CII] results were found to be invalid. Uncertainty maps, based on the scatter within the trimmed, uncollapsed data cloud, and

other diagnostic information maps are simultaneously produced using error propagation.

As a result of the late commissioning of the PACS unchopped line scan mode our data processing algorithms are still under development. At present we perform the fitting and integration on spectra with and without the off position removed, and combine the results using signal-to-noise criteria. We expect that as the understanding of how to perform the data deglitching improves this step, and the subtraction of the third order baseline will become obsolete and the maps will be reliably produced based on the off-subtracted data. In the future we will also correct the PACS data for long-term transient effects, which are expected with the Ge Ga detectors used in the spectrometer. Transients with time constants of a few hundred seconds are very noticeable in all detectors after a significant change in the background level (for example immediately following a calibration sequence, or after a move to a new position during a raster scan). The correction is performed as part of the standard PACS spectroscopy pipeline reduction in future versions of the HIPE reduction software (from HIPE 7.0), and we are exploring our own custom algorithms as well. Transients caused by cosmic ray hits on individual detector elements are not corrected by this technique, but these events are filtered out in the PACS pipeline using an outlier-rejection method which is very effective because of the huge degree of redundancy present in a typical observation with the spectrometer.

4.4. KINGFISH Data Deliveries

A staged delivery of complete PACS and SPIRE images and spectral line maps is planned as part of the KINGFISH project. The form of the projects is described above, and deliveries will be accompanied by full documentation. Since the time scale for completing the *Herschel* observations is uncertain it is not possible to produce a firm delivery schedule at this time. However the first set of KINGFISH data, comprising a complete set of processed SPIRE maps, was delivered to the HSC in June 2011, and should be available via the HSC User Reduced Data pages.⁴

5. A Taste of KINGFISH: Image Atlas, Sample Spectra, and SEDs

This paper is intended as an introduction and reference paper for the many science papers which we anticipate will follow from the KINGFISH team and from archival users

⁴<http://herschel.esac.esa.int/UserReducedData.shtml>

of the survey data. As illustrations of the scientific potential for these data, however, we present examples of early results from the imaging and spectroscopic observations.

To illustrate the wealth of information provided by the *Herschel* PACS+SPIRE maps, individually and in conjunction with *Spitzer* images, we present in Figure 7 montages of SINGS and KINGFISH images for all 61 galaxies in the KINGFISH sample. The printed edition shows an example for NGC 6946, with the nine panels depicting grayscale images in three *Spitzer* bands (3.6, 8.0, and 24 μm), the three *Herschel* PACS bands (70, 100, 160 μm), and the three SPIRE bands (250, 350, 500 μm). Images for all 61 galaxies can be found in the on-line version of this article. At the time this article was accepted PACS imaging had not yet been completed for NGC 584.

As a result of the late commissioning of the full PACS unchopped line scan mode (two years after launch) our spectroscopic observations are still in progress, and our data processing algorithms are still at an early stage of development. Nevertheless the powerful capabilities of these observations are illustrated in Figures 8 which show preliminary [CII], [OI], [NII], and [OIII] line maps and a velocity map for NGC 3521. Figure 9 shows spectra from representative regions that have been extracted from these maps.

We conclude with an illustration of how the sample size and diversity of the KINGFISH survey and the richness of its ancillary dataset can help to clarify and unravel some of the astrophysical questions raised in the first part of this paper.

Early studies of *IRAS*-selected samples had suggested that local galaxies tend to possess higher mean dust temperatures than high-redshift galaxies. This view has been slowly changing over the past decade, as more and more sub-mm data have been accumulating for significant local galaxies samples (e.g., Dunne & Eales 2001; Galliano et al. 2003, 2005; Dumke et al. 2004), thus extending the wavelength range to a regime that can probe the cold dust population and avoiding the earlier selection biases. Recent studies using submillimeter selected samples from *Blast* (Dye et al. 2009), *Herschel* (Boselli et al. 2010) or *Planck* (Planck Collaboration 2011) find that nearby galaxies exhibit colder temperatures than what was previously determined. The sub-mm excess of the local galaxies also is found to be more pronounced in metal-poor dwarf galaxies (e.g., O’Halloran et al. 2010, Galametz et al. 2010, 2011). Although the nature of the sub-mm excess in low metallicity galaxies is not yet fully known (e.g., Bot et al. 2010), studies of large samples such as that of Galametz et al. (2011), that combine infrared and sub-mm data, offer the best opportunity to investigate the systematics of the sub-mm excess emission.

The early *Herschel* KINGFISH data (Dale et al. 2011) offer an excellent opportunity to extend these studies of submillimeter dust by comparing with a consistent set of observations

the FIR–submillimeter SED shapes of the sample, and test whether these SEDs correlate systematically with the gross physical properties of the galaxies. As an illustration Figure 10 shows the dependence of the integrated $160\ \mu\text{m}/500\ \mu\text{m}$ flux density ratio as a function of the mean metal abundance, TIR luminosity, and TIR/FUV flux ratio (all plotted in logarithmic form). Significant correlations appear in all three comparisons, though the considerable uncertainties in individual mean metallicities make that a less convincing correlation than the others. Similar systematic trends in SED shape have been seen in early data from the *Herschel* Reference Survey (Boselli et al. 2010). These results show that the submillimeter emission *increases* as one goes from luminous, dusty and metal-rich galaxies to the more metal-poor dwarf galaxies, even though the SEDs of the latter often show indications of more warm dust at shorter wavelengths. It is tempting to associate the $160/500\ \mu\text{m}$ spectral slope as a proxy of the cold dust temperature, in which case the correlations in Figure 10 would suggest the presence of a larger amount of cold dust in low-metallicity environments. It is also possible however that the trends seen are produced by a systematic change in the emissivity properties of the dust. In either case the comparison suggests suggest a continuous trend rather than a dichotomy between the massive spiral and less massive dwarf galaxies.

This research has made use of the NASA/IPAC Extragalactic Database (NED) which is operated by the Jet Propulsion Laboratory, California Institute of Technology, under contract with the National Aeronautics and Space Administration.

REFERENCES

- Beirão, P. et al. 2010, A&A, 518, id.L60
- Bendo, G. et al. 2003, AJ, 125, 2361
- Bendo, G. et al. 2008, MNRAS, 389, 629
- Bigiel, F., Leroy, A., Walter, F., Brinks, E., de Blok, W.J.G., Madore, B., & Thornley, M.D. 2008, AJ, 136, 2846
- Blakeslee, J.P., Jordan, A., Mei, S., Cote, P., Ferrarese, L., Infante, L. et al. 2009, ApJ, 694, 556
- Boselli, A., Gavazzi, G., Lequeux, J., & Pierini, D. 2002, A&A, 385, 454
- Bolatto, A., Leroy, A.K., Rosolowsky, E., Walter, F., & Blitz, L. 2008, ApJ, 686, 948
- Boselli, A., et al. 2010a, PASP, 122, 261

- Boselli, A., et al. 2010b, *A&A*, 518, id.L61
- Bot, C., Ysard, N., Paradis, D., Bernard, J.P., Lagache, G., Israel, F.P., & Wall, W.F. 2010, *A&A*, 523, 20
- Braun, R., Oosterloo, T.A., Morganti, R., Klein, U., & Beck, R. 2007, *A&A*, 461, 455
- Brauhar, J.R., Dale, D.A., & Helou, G. 2008, *ApJS*, 178, 280
- Bresolin, F., Garnett, D. R., & Kennicutt, R. C. 2004, *ApJ*, 615, 228
- Bresolin, F., Gieren, W., Kudritzki, R.-P., Pietrzyński, G., Urbaneja, M. A., & Carraro, G. 2009, *ApJ*, 700, 309
- Calzetti, D., Harris, J., Gallagher, J.S., Smith, D.A., Conselice, C.J., Homeier, N., & Kewley, L. 2004, *AJ*, 127, 1405
- Calzetti, D. et al. 2005, *ApJ*, 633, 871
- Calzetti, D. et al. 2007, *ApJ*, 666, 870
- Calzetti, D. et al. 2010, *ApJ*, 714, 1256
- Cerviño, M., Luridiana, V., Pérez, E., Vílchez, J.M., & Valls-Gabaud, D. 2003, *A&A*, 407, 177
- Condon, J.J. 1992, *ARA&A*, 30, 575
- Contursi, A. et al. 2002, *AJ*, 124, 751
- Cortes, J.R., Kenney, J.D.P., & Hardy, E. 2008, *ApJ*, 683, 78
- Daigle, O., Carignan, C., Amram, P., Hernandez, O., Chemin, L., Balkowski, C., & Kennicutt, R. 2006, *MNRAS*, 367, 469
- Dalcanton, J.J., Williams, B.F., Seth, A.C., Dolphin, A., Holtzman, J., et al. 2009, *ApJS*, 183, 67
- Dale, D.A., & Helou, G. 2002, *ApJ*, 576, 159
- Dale, D.A., et al. 2007, *ApJ*, 655, 863
- Dale, D.A. et al. 2007, *ApJ*, 656, 770
- Dale, D.A. et al. 2009, *ApJ*, 693, 1821

- Dale, D.A. et al. 2009, *ApJ*, 703, 517
- Dale, D.A. et al. 2011, in preparation
- Deng, X.-F. 2010, *ApJ*, 721, 809
- de Vaucouleurs, G., de Vaucouleurs, A., Corwin, H.G., Buta, R.J., Paturel, G., & Fouqué, P. 1991, *Third Reference Catalog of Bright Galaxies*, Austin, University of Texas Press
- Dicaire, I. et al. 2008, *MNRAS*, 385, 553
- Diolaiti, E., Bendinelli, O., Bonaccini, D., Close, L., Currie, D., & Parmeggiani, G. 2000, *A&AS*, 147, 335
- Draine, B.T. et al. 2007, *ApJ*, 663, 866
- Draine, B.T., & Li, A. 2007, *ApJ*, 657, 810
- Drozdosky, I.O., & Karachentsev, I.D. 2000, *A&AS*, 142, 425
- Dumke, R., Krause, M., & Wielebinski, R. 2004, *A&A*, 414, 475
- Dunne, L. & Eales, S.A. 2001, *MNRAS*, 327, 697
- Dye, S. et al. 2009, *ApJ*, 703, 285
- Engelbracht, C.W. et al. 2006, *ApJ*, 642, L127
- Engelbracht, C.W., Rieke, G.H., Gordon, K.D., Smith, J.D.T., Werner, M.W., Moustakas, J., Willmer, C.N.A., & Vanzi, L. 2008, *ApJ*, 678, 804
- Engelbracht, C.W. et al. 2010, *A&A*, 518, id.L56
- Flower, D.R., & Pineau Des Forêts 2010, *MNRAS*, 406, 1745
- Förster Schreiber, N.M., Roussel, H., Sauvage, M., & Charmandaris, V. 2004, *A&A*, 419, 501
- Freedman, W.L., Madore, B.F., Gibson, B.K., Ferrarese, L., Kelson, D.D., et al. 2001, *ApJ*, 553, 47
- Galametz, M. et al. 2010, *A&A*, 580, L55
- Galametz, M., Madden, S.C., Galliano, F., Hony, S., Bendo, G.J., & Sauvage, M. 2011, *A&A*, 532, 56

- Galliano, F., Madden, S.C., Jones, A.P., Wilson, C.D., Bernard, J.-P., Le Peindre, F. 2003, *A&A*, 407, 159
- Galliano, F., Madden, S.C., Jones, A.P., Wilson, C.D., & Bernard, J.-P. 2005, *A&A*, 434, 867
- Gil de Paz, A. et al. 2007, *ApJS*, 173, 185
- Gordon, K.D. et al. 2010, *A&A*, 518, id.L89
- Gracia-Carpio, J. et al. 2011, *ApJ*, 728, L7
- Griffin, M.J. et al. 2010, *A&A*, 518, id.L3
- Haas, M., Klaas, U., & Bianchi, S. 2002, *A&A*, 385, L23
- Helou, G., Soifer, B.T., & Rowan-Robinson, M. 1985, *ApJ*, 298, L7
- Helou, G., Lu, N.Y., Werner, M.W., Malhotra, S., & Silbermann, N. 2000, *ApJ*, 532, 21
- Helou, G., Malhotra, S., Hollenbach, D.J., Dale, D.A., & Contursi, A. 2001, *ApJ*, 548, L73
- Helou, G. et al. 2004, *ApJS*, 154, 253
- Hinz, J.L. et al. 2004, *ApJS*, 154, 259
- Hinz, J.L., Misselt, K., Rieke, M.J., Rieke, G.H., Smith, P.S., Blaylock, M., & Gordon, K.D. 2006, *ApJ*, 651,
- Ho, L.C., Filippenko, A.V., & Sargent, W.L.W. 1997, *ApJS*, 112, 315
- Hoessel, J.G., Saha, A., Danielson, G.E. 1998, *AJ*, 115, 573
- Hollenbach, D.J., & Tielens, A.G.G.M. 1997, *ARA&A*, 35, 179
- Hollenbach, D.J., & Tielens, A.G.G.M. 1999, *Reviews of Modern Physics*, 71, 173
- Israel, F. P., Wall, W. F., Raban, D., Reach, W. T., Bot, C., Oonk, J. B. R., Ysard, N., & Bernard, J. P. 2010, *A&A*, 519, A67, 874
- Jarrett, T. H., Chester, T., Cutri, R., Schneider, S. E., & Huchra, J. P. 2003, *AJ*, 125, 525
- Jenkins, L. et al. 2011, *HEAD*, 11, 2905
- Jensen, J.B., Tonry, J.L., Barris, B.J., Thompson, R.I., Liu, M.C., Rieke, M.J., et al. 2003, *ApJ*, 583, 712

- Jones, M.I., Hamuy, M., Lira, P., Maza, J., Clocchiatti, A., Phillips, M. et al. 2009, *ApJ*, 696, 1176
- Kanbur, S.M., Ngeow, C., Nikolaev, S., Tanvir, N.R., & Hendry, M.A. 2003, *A&A*, 411, 361
- Karachentsev, I.D., Sharina, M.E., & Huchmeier, W.K. 2000, *A&A*, 362, 544
- Karachentsev, I.D., Dolphin, A.E., Geisler, D., Grebel, E.K., Guhatakurta, P., et al. 2002, *A&A*, 383, 125
- Karachentsev, I.D., Sharina, M.E., Dolphin, A.E., Grebel, E.K., Geisler, D., et al. 2002, *A&A*, 385, 21
- Karachentsev, I.D., Sharina, M.E., Dolphin, A.E., Grebel, E.K., Geisler, D., et al. 2003, *A&A* 398, 467
- Karachentsev, I.D., Makarov, D.I., Sharina, M.E., Dolphin, A.E., Grebel, E.K., et al. 2003, *A&A* 398, 479
- Karachentsev, I.D., Grebel, E.K., Sharina, M.E., Dolphin, A.E., Geisler, D., et al. 2003, *A&A*, 404, 93
- Kaufman, M.J., Wolfire, M.G., Hollenbach, D.J., & Luhman, M.L. 1999, *ApJ*, 527, 795
- Kaufman, M.J., Wolfire, M.G., & Hollenbach, D.J. 2006, *ApJ*, 644, 283
- Kennicutt, R.C. 1998a, *ARA&A*, 36, 189
- Kennicutt, R.C. 1998b, *ApJ*, 498, 541
- Kennicutt, R.C., Bresolin, F., & Garnett, D.R. 2003, *ApJ*, 591, 801
- Kennicutt, R.C. et al. 2003, *PASP*, 115, 928
- Kennicutt, R.C. et al. 2007, *ApJ*, 671, 333
- Kennicutt, R.C., Lee, J.C., Funes, J.G., Sakai, S., & Akiyama, S. 2008, *ApJS*, 178, 247
- Kennicutt, R.C. et al. 2009, *ApJ*, 703, 1672
- Kewley, L.J., & Ellison, S.L. 2008, *ApJ*, 681, 1183
- Kobulnicky, H.A., & Kewley, L.J. 2004, *ApJ*, 617, 240
- Lagache, G., Puget, J.-L., & Dole, H. 2005, *ARA&A*, 43, 727

- Lawton, B. et al. 2010, ApJ, 716, 453
- Lee, J.C. et al. 2009, ApJ, 706, 599
- Leroy, A., Bolatto, A., Stanimirovic, S., Mizuno, N., Israel, F., & Bot, C. 2007, ApJ, 658, 1027
- Leroy, A.K., Walter, F., Brinks, E., Bigiel, F., de Blok, W.J.G., Madore, B., & Thornley, M.D. 2008, AJ, 136, 2782
- Leroy, A.K. et al. 2009, AJ, 137, 4670
- Leroy, A. K., et al. 2009, ApJ, 702, 352
- Leroy, A.K. et al. 2011, ApJ, 737, 12
- Li, Y., Calzetti, D., Kennicutt, R.C., Hong, S., Engelbracht, C.W., Dale, D.A., & Moustakas, J. 2010, ApJ, 725, 677
- Lisenfeld, U., Israel, F.P., Stil, J.M., & Sievers, A. 2002, A&A, 382, 860
- Liu, G., Koda, J., Calzetti, D., Fukuhara, M., & Momose, R. 2011, ApJ, 735, 63
- Makarova, L., Karachentsev, I., Takalo, L.O., Heinaemaeki, P., & Valtonen, M. 1998, A&AS, 128, 459
- Malhotra, S. et al. 1997, ApJ, 491, L27
- Malhotra, S. et al. 2001, ApJ, 543, 634
- Marleau, F.R. et al. 2006, ApJ, 646, 929
- Martin, C.L., & Kennicutt, R.C. 2001, ApJ, 555, 301
- McQuinn, K.B.W. et al. 2010a, ApJ, 721, 297
- McQuinn, K.B.W. et al. 2010b, ApJ, 724, 49
- Meijerink, R., Tilanus, R.P.J, Dullemond, C.P., Israel, F.P., & van der Werf, P.P. 2005, A&A, 430, 427
- Meijerink, R., Spaans, M., & Israel, F.P. 2007, A&A, 461, 793
- Meixner, M. et al. 2010, A&A, 518, id.L71
- Meurer, G. et al. 2009, ApJ, 695, 765

- Mould, J., & Sakai, S. 2008, *ApJ*, 686, L75
- Moustakas, J., Kennicutt, R. C., Jr., Tremonti, C. A., Dale, D. A., Smith, J.-D. T., & Calzetti, D. 2010, *ApJS*, 190, 233
- Muñoz-Mateos, J.C. et al. 2009a, *ApJ*, 701, 1965
- Muñoz-Mateos, J.C. et al. 2009b, *ApJ*, 703, 1569
- Murphy, E.J. 2006a, *ApJ*, 638, 157
- Murphy, E.J. 2006b, *ApJ*, 651, L111
- Murphy, E.J., Helou, G., Kenney, J.D.P., Armus, L., & Braun, R. 2008, *ApJ*, 678, 828
- Murphy, E.J. et al. 2011, *ApJ*, 737, 67
- Nguyen, H. T., et al. 2010, *A&A*, 518, id.L5
- O’Halloran, B. et al. 2010, *A&A*, 518, id.L58
- Ott, S. 2010, in *Astronomical Data Analysis Software and Systems XIX.*, eds. Y. Mizumoto, K.-I. Morita, & M. Ohishi, *ASP Conf Ser*, 434, 139
- Pérez-gonzález, P.G. et al. 2006, *ApJ*, 648, 987
- Pérez-Montero, E., & Díaz, A.I. 1995, *MNRAS*, 361, 1063
- Pilbratt, G.L. et al. 2010, *A&A*, 518, id.L1
- Pilyugin, L.S., Vilchez, J.M., & Contini, T. 2004, *A&A*, 425, 849
- Pilyugin, L.S., & Thuan, T.X. 2005, *ApJ*, 631, 231
- Planck Collaboration 2011a, *arXiv:1101.2045*
- Planck Collaboration 2011b, *arXiv:1101.2046*
- Poglitsch, A. et al. 2010, *A&A*, 518, id.L2
- Poznanski, D., Nathaniel, B., Filippenko, A.V., Ganeshalingam, M., Li, W., et al. 2009, *ApJ*, 694, 1067
- Prescott, M.K.M. et al. 2007, *ApJ*, 668, 182

- Rieke, G. H., Alonso-Herrero, A., Weiner, B. J., Pérez-González, P. G., Blaylock, M., Donley, J. L., & Marcillac, D. 2009, *ApJ*, 692, 556
- Rodriguez-Fernandez, N. J., Braine, J., Brouillet, N., & Combes, F. 2006, *A&A*, 453, 77
- Roussel, H., Sauvage, M., Vigroux, L., & Bosma, A. 2001, *A&A*, 372, 427
- Roussel, H. et al. 2007, *ApJ*, 669, 959
- Roussel, H. 2011, *A&A*, submitted
- Rudolph, A. L., Fich, M., Bell, G. R., Norsen, T., Simpson, J. P., Haas, M. R., & Erickson, E. F. 2006, *ApJS*, 162, 346
- Saha, A., Claver, J., & Hoessel, J.G. 2002, *AJ*, 124, 839
- Saha, A., Thim, F., Tamman, G.A., Reindl, B., & Sandage, A. 2006, *ApJS*, 165, 108
- Salim, S. et al. 2007, *ApJS*, 173, 267
- Sandstrom, K. et al. 2010, *A&A*, 518, id.L59
- Seth, A.C., Dalcanton, J.J., & de Jong, R.S. 2005, *AJ*, 129, 1331
- Skibba, R. et al. 2011, *ApJ*, 738, 89
- Soifer, B.T., Neugebauer, G., & Houck, J.R. 1987, *ARA&A*, 25, 187
- Soifer, B. T., Boehmer, L., Neugebauer, G., & Sanders, D. B. 1989, *AJ*, 98, 766
- Soifer, B.T., Helou, G., & Werner, M. 2008, *ARA&A*, 46, 201
- Springob, C.M., Masters, K.L., Haynes, M.P., Giovanelli, R., & Marinoni, C. 2009, *ApJS*, 182, 474
- Strong, A.W., Moskalenko, I.V., Reimer, O., Digel, S., & Diehl, R. 2004, *A&A*, 422, L47
- Tonry, J.L., Dressler, A., Blakeslee, J.P., Ajhar, E.A., Fletcher, A.B., et al. 2001, *ApJ*, 546, 681
- Tully, R.B. 1988, *Nearby Galaxy Catalog*, Cambridge, CUP
- Tully, R.B., Rizzi, L., Shaya, E.J., Courtois, H.M., Makarov, D.I., & Jacobs, B.A. 2009, *AJ*, 138, 323
- Van Dyk, S.D., Li, W., & Filippenko, A.V. 2006, *PASP*, 118, 351

Walter, F., Brinks, E., de Blok, W. J. G., Bigiel, F., Kennicutt, R. C., Thornley, M. D., & Leroy, A. 2008, *AJ*, 136, 2563

Walter, F. et al. 2009, *Nature*, 457, 699

Walter, F. et al. 2011, *ApJ*, 726, L11

Weisz, D.R. et al. 2011, *ApJ*, 739, 5

Willick, J.A., Courteau, S., Faber, S.M., Burstein, D., Dekel, A., & Strauss, M.A. 1997, *ApJS*, 109, 333

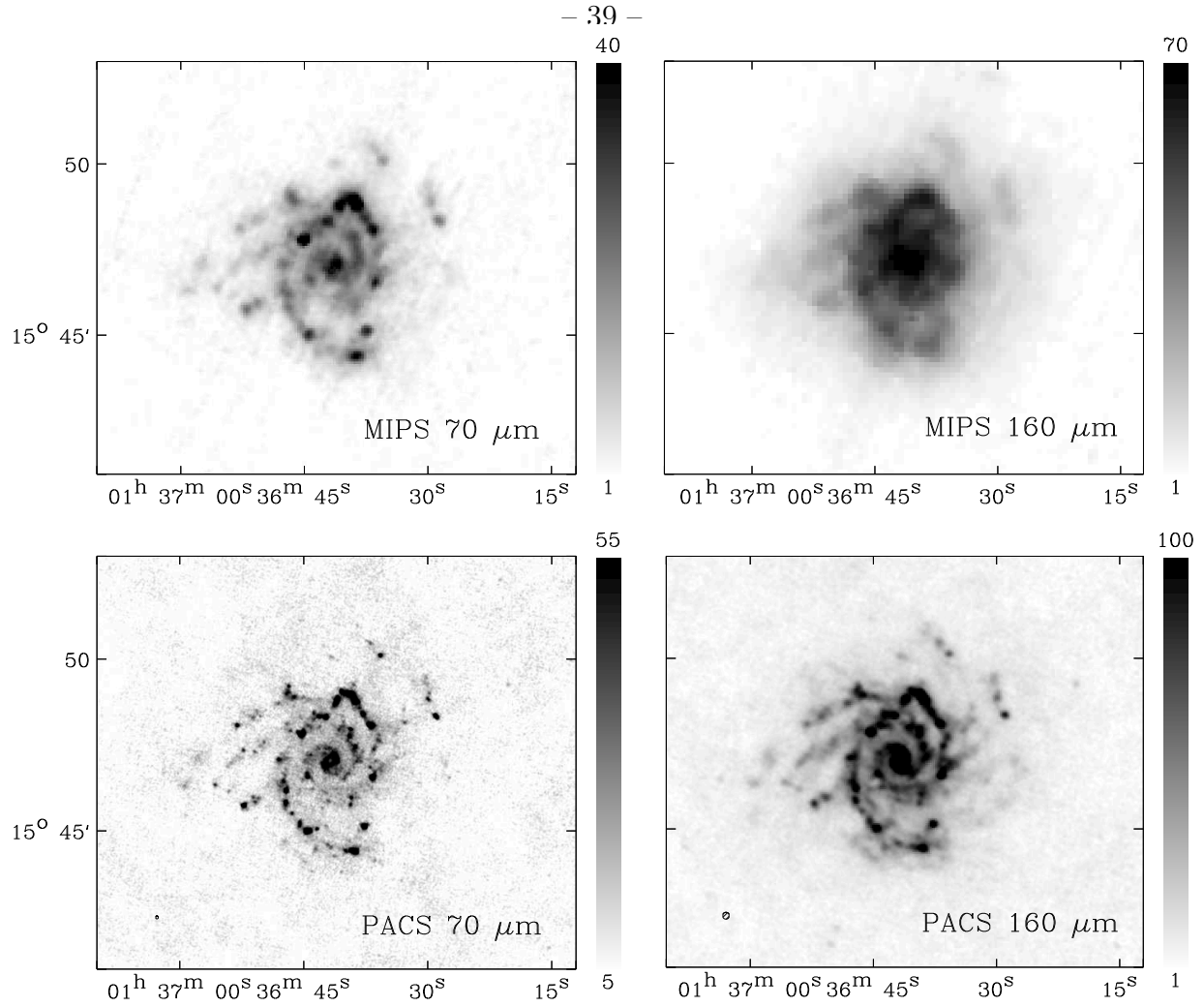


Fig. 1.— Top: Far-infrared scan maps of the KINGFISH galaxy NGC 628 at 70 μm (left) and 160 μm (right), as observed with the *Spitzer* MIPS instrument as part of the SINGS project. Bottom: Scan maps at the same wavelengths with the *Herschel* PACS imager, and processed using the Scanamorphos mapping package. The superior spatial resolution of the PACS images is readily apparent, though the MIPS maps should still be more sensitive to faint extended emission.

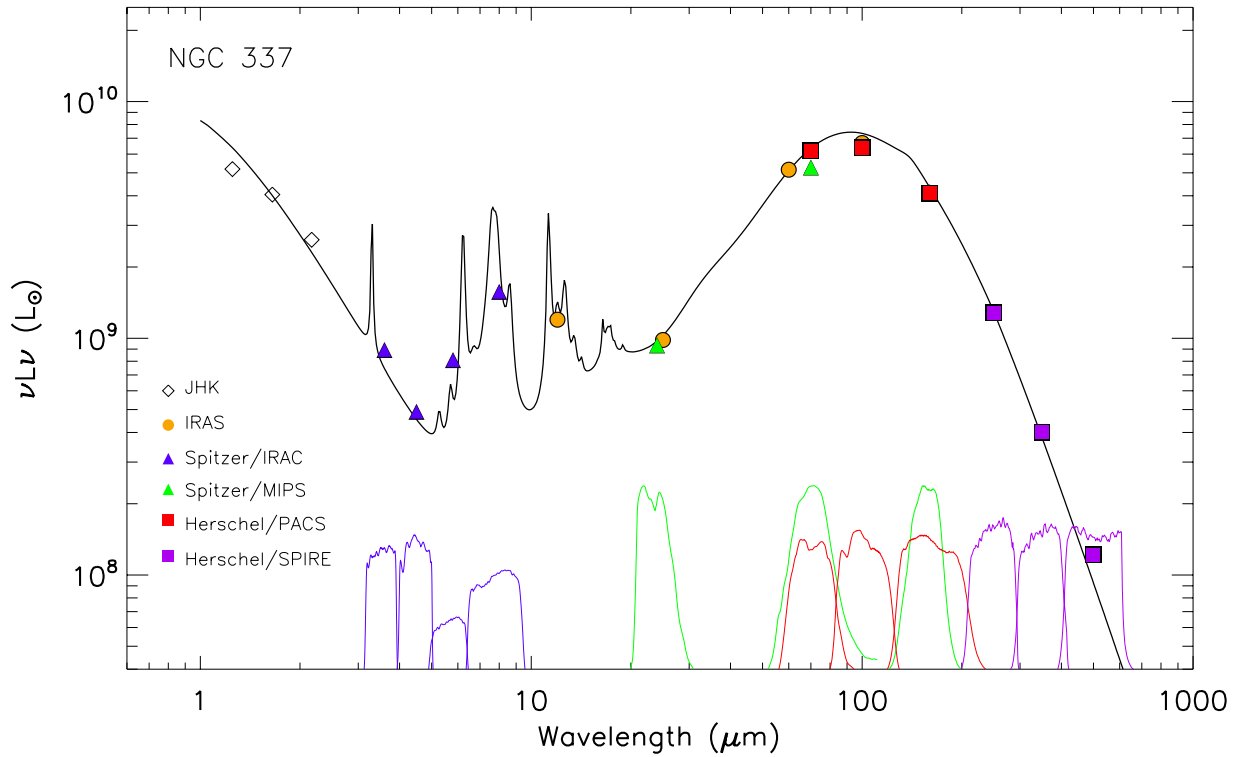


Fig. 2.— Integrated spectral energy distribution (SED) for the KINGFISH galaxy NGC 337, based on combined measurements with the *Spitzer* IRAC and MIPS instruments, and the *Herschel* PACS and SPIRE instruments. The corresponding filter bandpasses are shown at the bottom of the figure. The dark line is a fit of a dust model following Draine et al. (2007). Note the importance of the SPIRE fluxes in the 250–500 μm region for constraining the SED shape at long wavelengths.

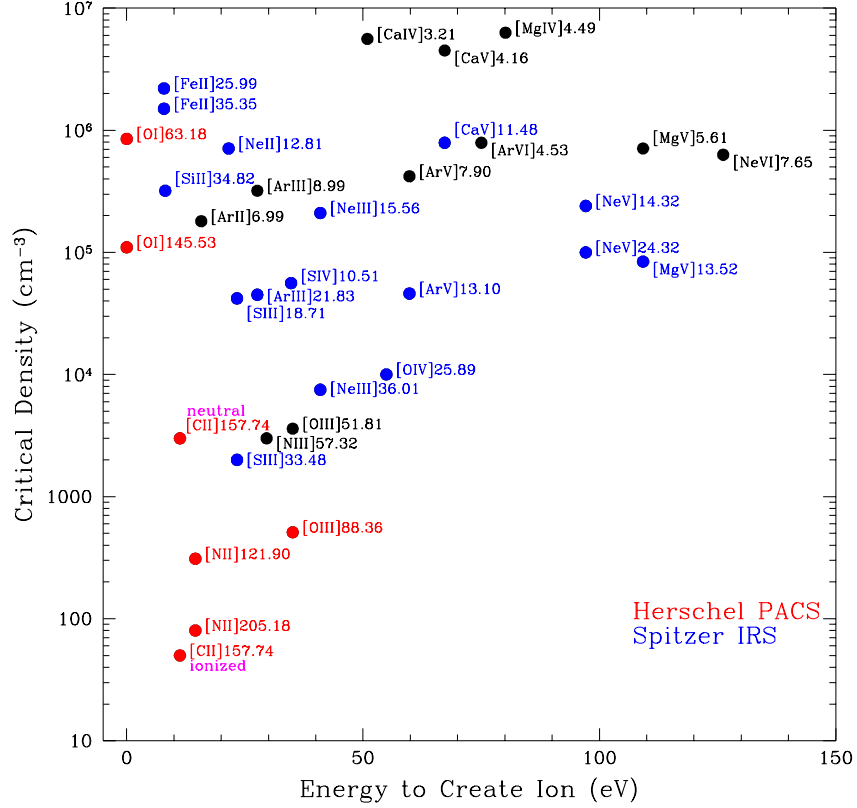


Fig. 3.— Key diagnostic lines for the ISM, in terms of ionization potential and critical density. Red points denote lines accessible within the spectral range of the *Herschel* PACS spectrometer, while blue points show lines that lie within the spectral coverage of the *Spitzer* IRS instrument. Black points fall outside of the sensitive range of either instrument but are shown for completeness. The two critical densities shown for the [CII] 158 μ m line apply to collisional de-excitations from electrons (ionized regions) and from atoms (neutral regions). Note the unique range of conditions that are probed by the primary far-infrared cooling lines from *Herschel*. All of the lines shown in red except for [OI] 145.5 μ m are being observed as part of KINGFISH.

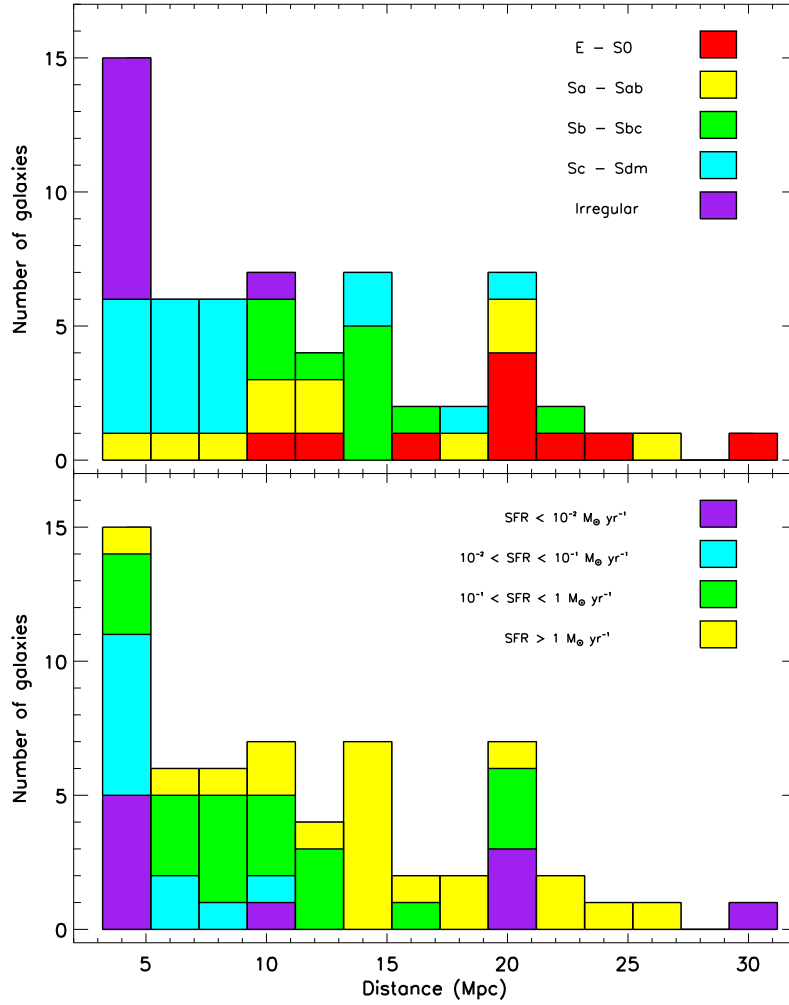


Fig. 4.— Above: Distribution of KINGFISH galaxies by morphological type and distance. Below: Distribution by star formation rate (as derived from a combination of $H\alpha$ and $24 \mu m$ measurements) and distance.

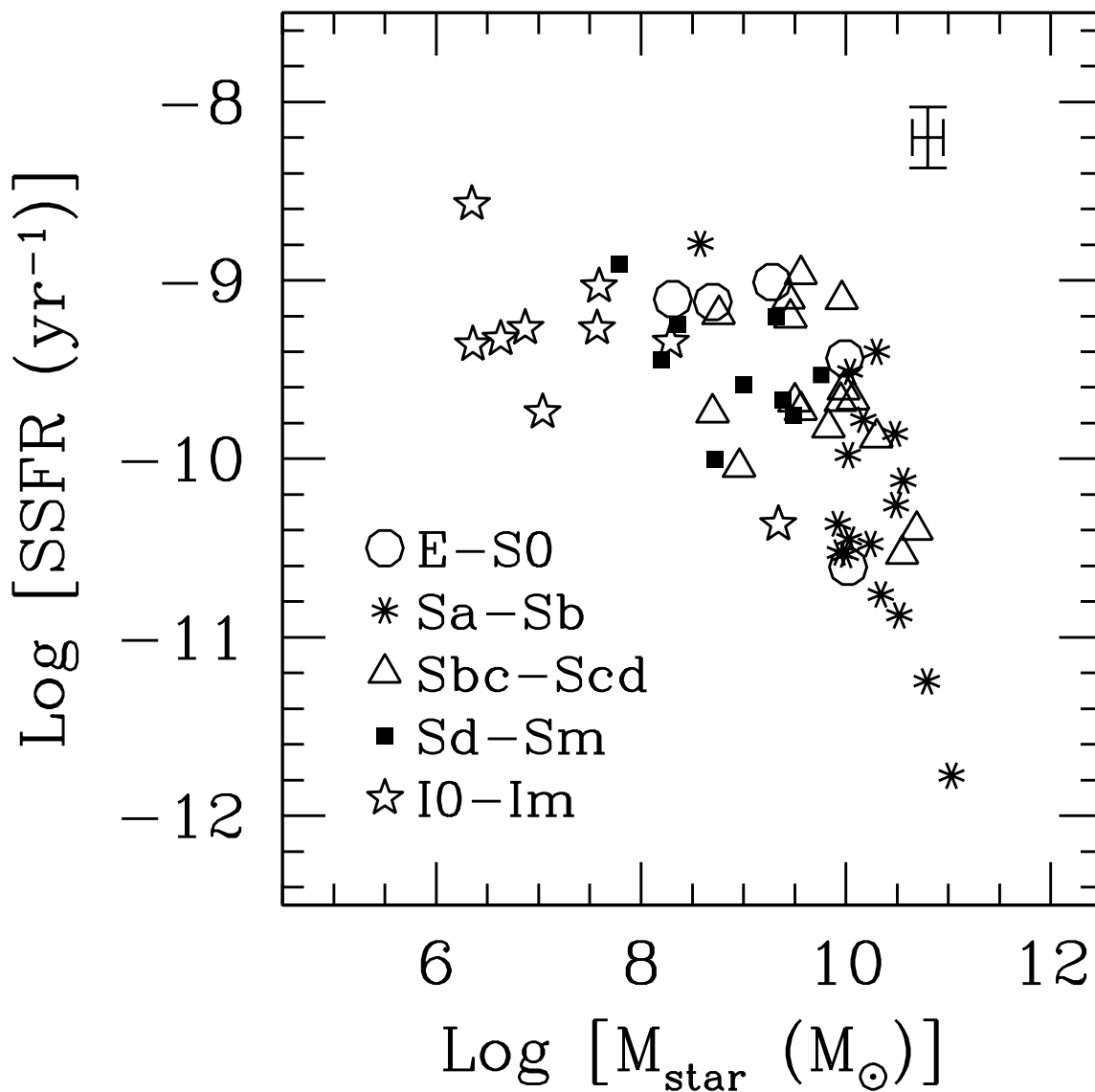


Fig. 5.— Specific star formation rate for KINGFISH galaxies, $\text{SSFR} = \text{SFR}/M_{\text{star}}$, where the SFR and the stellar mass M_{star} are from Table 1. Only galaxies for which a SFR is available are shown on the plot. A representative 1σ error bar is shown in the top-right corner of the figure. The error bar includes only random errors (Skibba et al. 2001).

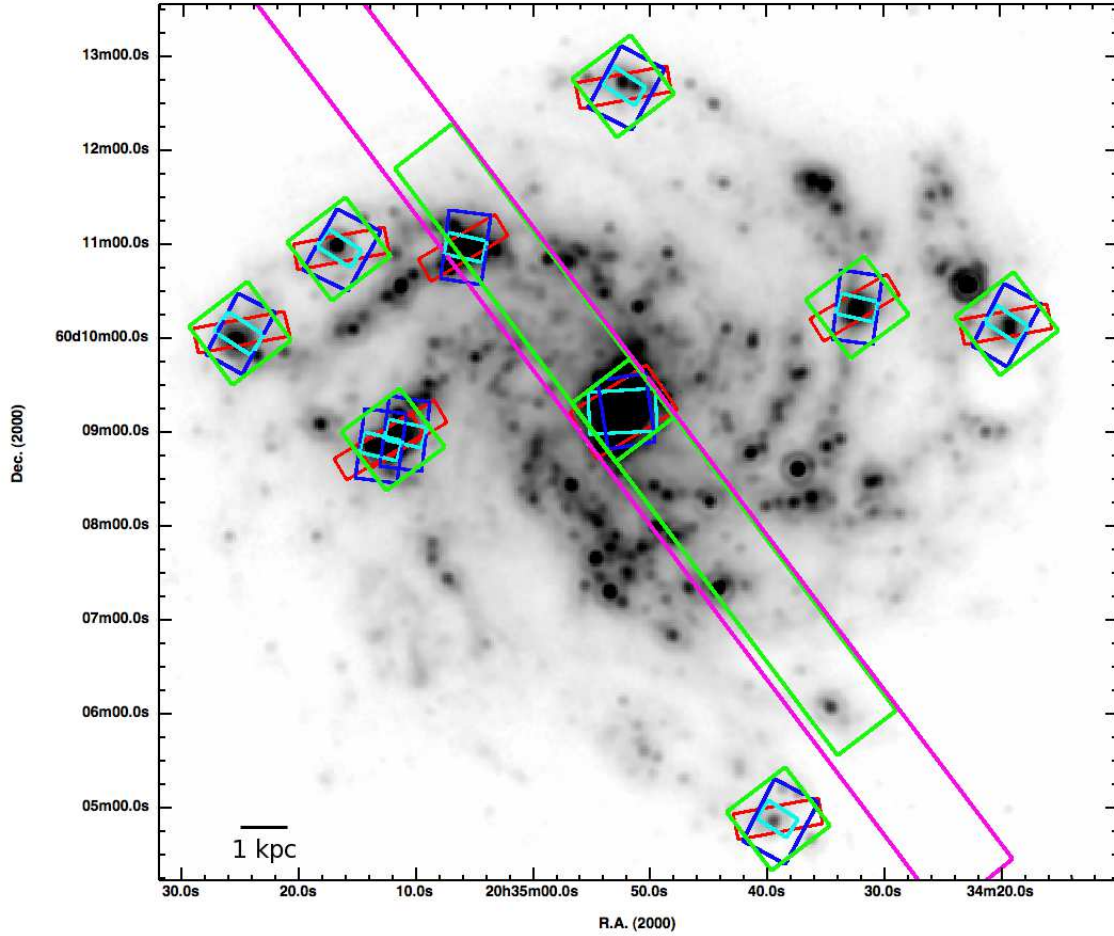


Fig. 6.— *Spitzer* 8 μm image of NGC 6946, with PACS spectroscopic line imaging regions superimposed (green boxes). The other color boxes show the footprints of the corresponding *Spitzer* IRS observations from SINGS: 5–14 μm low resolution spectral maps (red); 14–38 μm low resolution maps (magenta); and 10–37 μm high-resolution spectral maps (cyan and blue).

NGC 6946 (6.8 Mpc, SABcd)

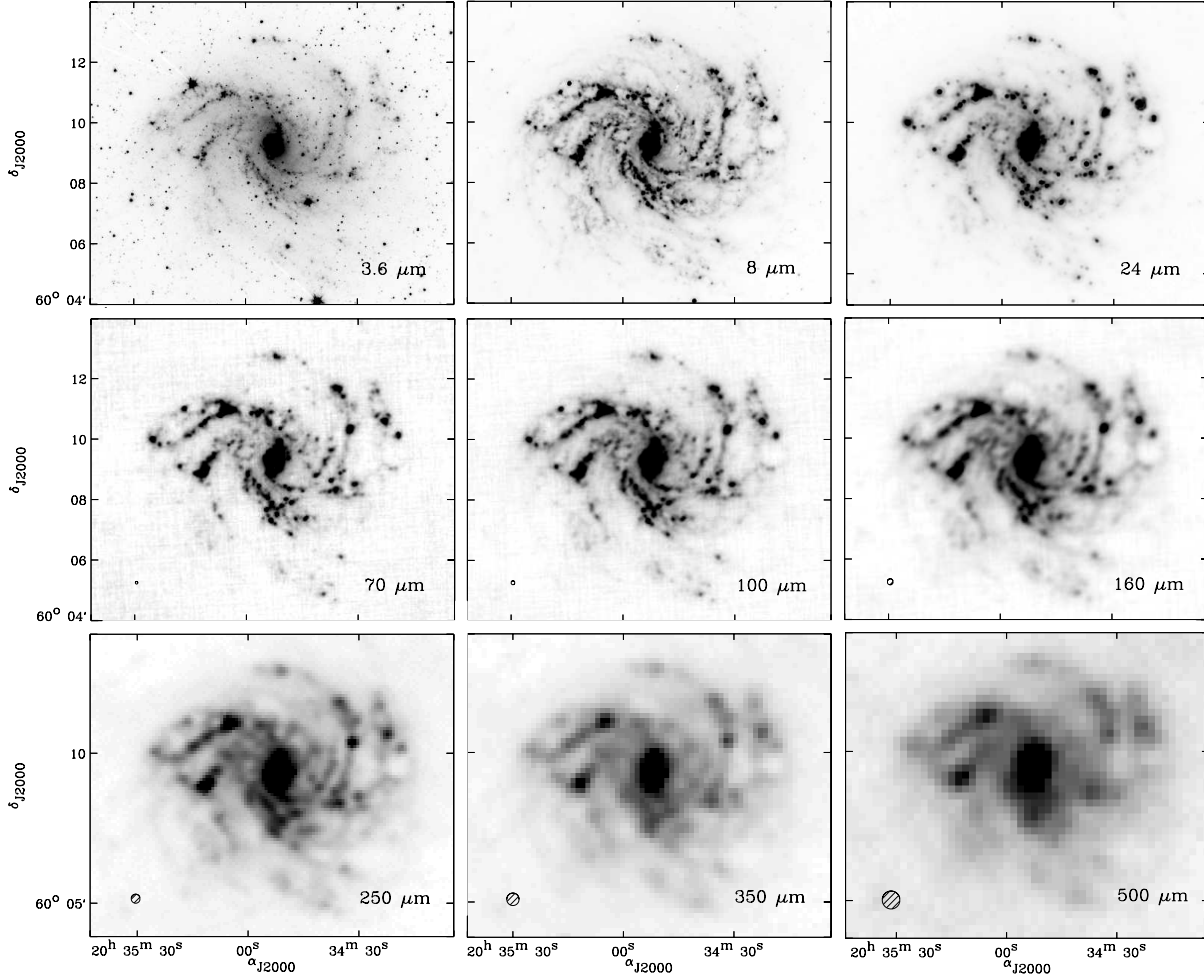


Fig. 7.— A montage of infrared images of NGC 6946 from *Spitzer* (SINGS) and *Herschel* (KINGFISH). FWHM beam sizes for the respective *Herschel* bands are shown in the lower left corner of each panel. *Top panels:* *Spitzer* IRAC images at 3.6 μm and 8.0 μm , and MIPS image at 24 μm . The emission at these wavelengths is dominated by stars, small PAH dust grains, and small dust grains heated by intense radiative fields, respectively. *Middle panels:* *Herschel* PACS images at 70 μm , 100 μm , and 160 μm , processed with the Scanamorphos map making package. Note the excellent spatial resolution despite the longer wavelengths, and the progressive increase in contributions from diffuse dust emission (“cirrus”) with increasing wavelength. *Bottom panels:* *Herschel* SPIRE images at 250 μm , 350 μm , and 500 μm . These bands trace increasingly cooler components of the main thermal dust emission, with possible additional contributions from “submillimeter excess” emission at the longest SPIRE wavelengths. A figure set with similar images for all 61 galaxies in the KINGFISH sample can be found in the on-line version of this article.

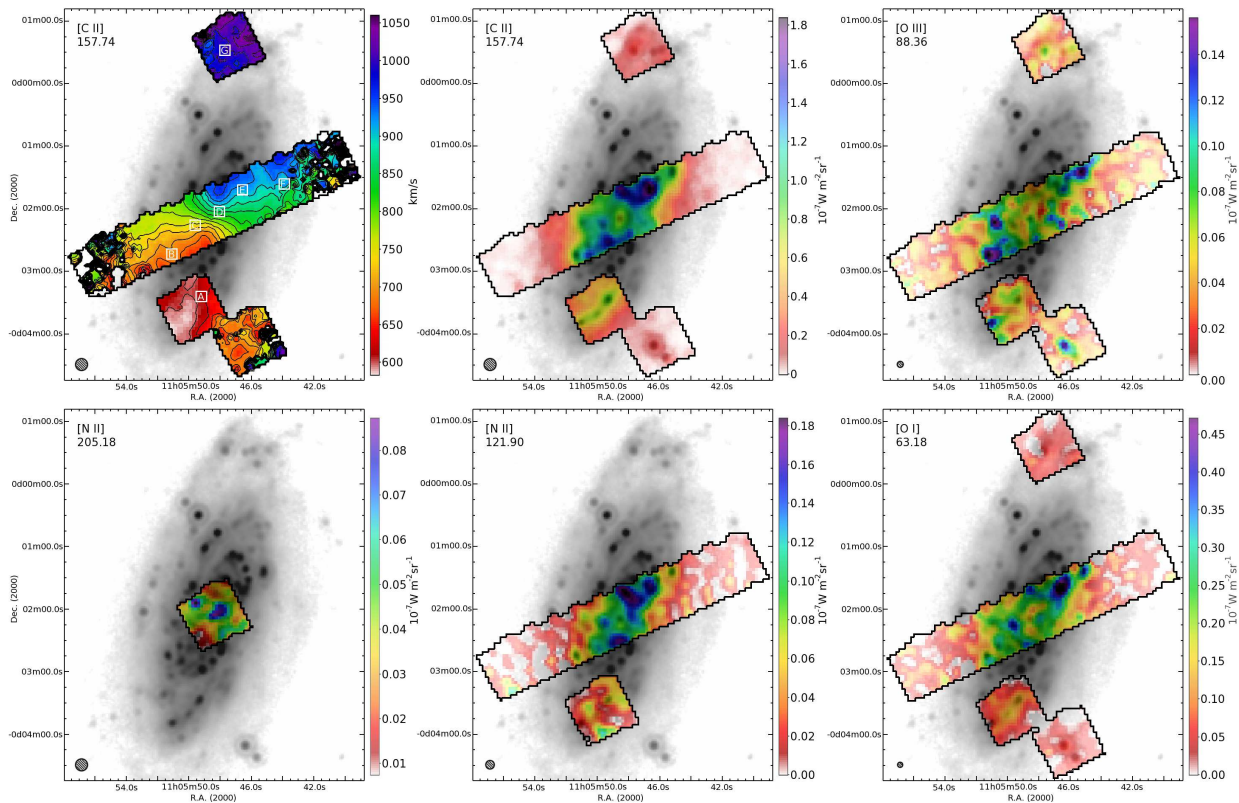


Fig. 8.— Line maps of [CII], [OIII], the two [NII] lines, and [OI] from KINGFISH observations of NGC 3521. The line maps are overlaid on the SINGS MIPS 24 μm image, and clipped at an RMS level of 3σ . The top left panel shows radial velocities as measured from the [CII] line (color and contours), while the other panels show line flux, in units given by the respective color bars. Note the range of flux between different lines. The white boxes in the top left panel indicate the extraction apertures for the line profiles that are shown in Figure 9.

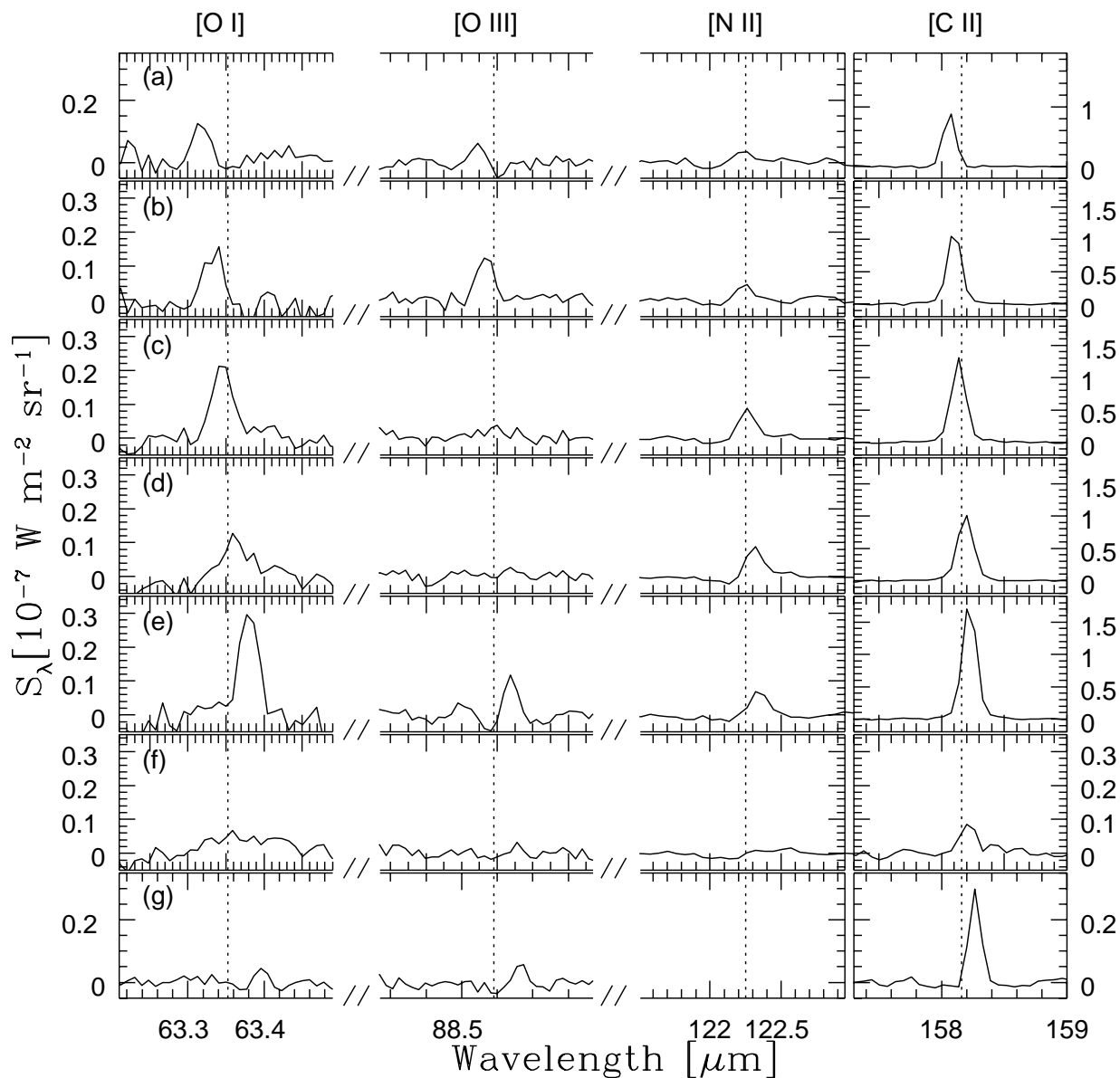


Fig. 9.— Spectra of [OI], [OIII], [NII], and [CII] are shown for representative apertures (Figure 8) extracted from KINGFISH observations of NGC 3521. Apertures cover a range of surface brightness and environments, e.g., diffuse gas and HII regions. The vertical lines show the expected position of the lines at the systemic velocity of NGC 3521; the offsets are caused by the rotation of the galaxy.

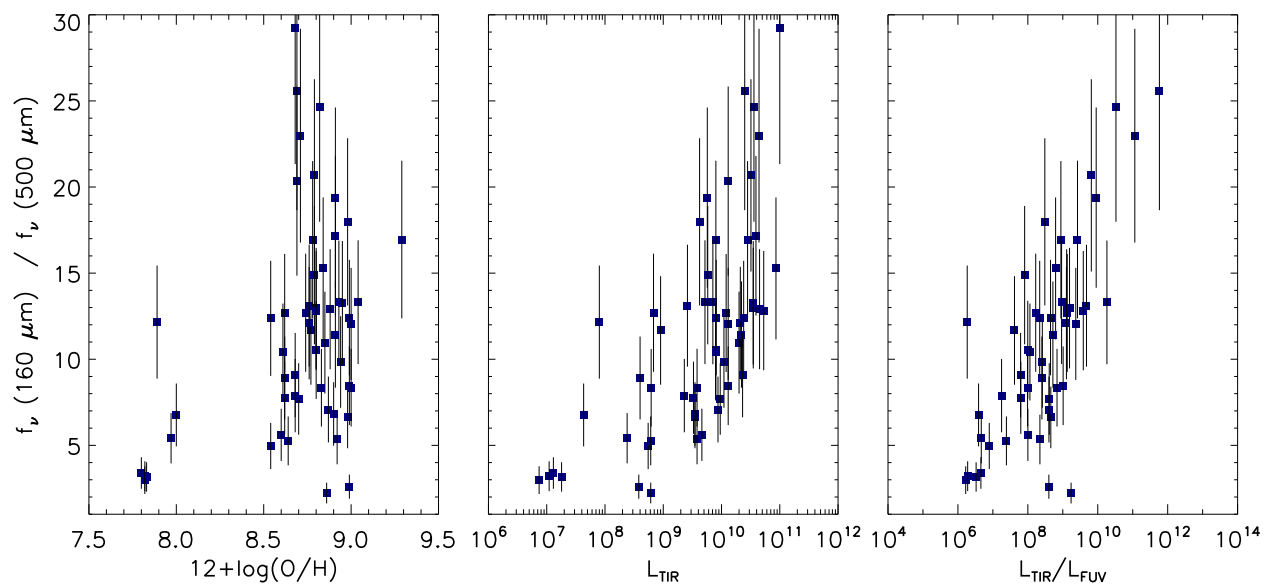


Fig. 10.— Ratio of integrated $160\ \mu\text{m}$ flux density (MIPS) to $500\ \mu\text{m}$ flux density (SPIRE) for the KINGFISH galaxies, plotted as functions of mean disk metal abundance total infrared luminosity, and infrared to far-ultraviolet (153 nm) flux ratio, an approximate measure of total dust obscuration. Note the strong trends, in sense of increased submillimeter emission and thus *colder* dust SEDs in the fainter, less dusty, and more metal-poor lower-mass galaxies.

Table 1. Properties of the KINGFISH Galaxies Sample.

Name ^a	v_H^a (km s ⁻¹)	Morph. ^a	Sizes ^a ($'\times'$)	Dist. ^b (Mpc)	Method ^c	Ref ^d	Nuc. Type ^e	12+log(O/H) ^f (PT)	(KK)	L _{3.6} ^g (L _⊙)	L _{TIR} ^h (L _⊙)	SFR ⁱ (M _⊙ yr ⁻¹)	M _* ^j (M _⊙)	PACS/SPIRE ^k
(1)	(2)	(3)	(4)	(5)	(6)	(7)	(8)	(9)	(10)	(11)	(12)	(13)	(14)	(15)
NGC0337	1650	SBd	2.9×1.8	19.3	TF	1	SF	8.18	8.84	9.4E8	1.2E10	1.30	9.32	B
NGC0584	1854	E4	4.2×2.3	20.8	SBF	2	...	8.43(+)	9.07(+)	4.2E9	6.1E8	...	11.12	F
NGC0628	657	SAC	10.5×9.5	7.2	SNII	3	...	8.35	9.02	1.2E9	8.0E9	0.68	9.56	B
NGC0855	610	E	2.6×1.0	9.73	SBF	2	SF	8.29	8.80	1.1E8	4.0E8	...	8.67	B
NGC0925	553	SABd	10.5×5.9	9.12	Ceph	4	SF	8.25	8.79	6.7E8	4.6E9	0.54	9.49	F
NGC1097	1275	SBb	9.3×6.3	14.2	TF	5	AGN	8.47	9.09	6.5E9	4.5E10	4.17	10.48	B
NGC1266	2194	SB0	1.5×1.0	30.6	TF	6	AGN	8.29(+)	8.89(+)	1.3E9	2.5E10	...	10.14	B
NGC1291	839	SBa	9.8×8.1	10.4	TF	6	AGN	8.52(+)	9.20(+)	5.9E9	3.5E9	0.35	10.79	B
NGC1316	1760	SAB0	12.0×8.5	21.0	SBF	7	AGN	8.77(+)	9.52(+)	2.9E10	8.0E9	...	11.46	F
NGC1377	1792	S0	1.8×0.9	24.6	TF	6	...	8.29(+)	8.89(+)	9.0E8	1.3E10	1.86	9.28	B
NGC1404	1947	E1	3.3×3.0	20.2	SBF	7	...	8.54(+)	9.21(+)	7.8E9	3.8E8	...	10.88	F
IC342	31	SABcd	21.4×20.	3.28	Ceph	8	SF(*)	8.49(P)	...	2.5E9(E)	1.4E10	1.87	9.95	B
NGC1482	1655	SA0	2.5×1.4	22.6	TF	6	SF	8.11	8.95	2.8E9	4.4E10	3.57	9.99	B
NGC1512	896	SBab	8.9×5.6	11.6	TF	1	AGN	8.56	9.11	1.4E9	3.8E9	0.36	9.92	F
NGC2146	893	Sbab	6.0×3.4	17.2	TF	9	SF(*)	8.68(E)	...	7.3E9(E)	1.0E11	7.94	10.30	F
HoII	157	Im	7.9×6.3	3.05	Ceph	10	...	7.72	8.13	1.7E7	8.0E7	0.036	7.59	F
DDO053	19	Im	1.5×1.3	3.61	TRGB	11	...	7.60	8.00	1.7E6	1.3E7	0.006	6.35	B
NGC2798	1726	SBa	2.6×1.0	25.8	TF	6	SF/AGN	8.34	9.04	1.9E9	3.6E10	3.38	10.04	B
NGC2841	638	SAb	8.1×3.5	14.1	Ceph	12	AGN	8.54	9.21	6.6E9	1.3E10	2.45	10.17	B
NGC2915	468	I0	1.9×1.0	3.78	TRGB	13	SF	7.94	8.28	2.0E7	4.3E7	0.020	7.57	F
HoI	143	IABm	3.6×3.0	3.9	TRGB	11	...	7.61	8.04	4.8E6	1.8E7	0.004	6.87	B
NGC2976	3	SAC	5.9×2.7	3.55	TRGB	11	SF	8.36	8.98	1.4E8	9.0E8	0.082	8.96	B
NGC3049	1494	SBab	2.2×1.4	19.2	TF	6	SF	8.53	9.10	3.8E8	3.5E9	0.61	8.58	B
NGC3077	14	I0pec	5.4×4.5	3.83	TRGB	11	SF(*)	...	8.9:(C)	2.1E9(D)	6.4E8	0.094	9.34	F
M81DwB	350	Im	0.9×0.6	3.6 ^l	M81G	7.84	8.19	1.7E6	6.8E6	0.001	6.36	B
NGC3190	1271	SAap	4.4×1.5	19.3	TF	6	AGN(*)	8.49(+)	9.15(+)	3.6E9	7.1E9	0.38	10.03	B
NGC3184	592	SABcd	7.4×6.9	11.7	SNII	14	SF	8.51	9.15	2.0E9	1.1E10	0.66	9.50	B
NGC3198	663	SBc	8.5×3.3	14.1	Ceph	15	SF	8.34	8.90	1.4E9	9.5E9	1.01	9.83	F
IC2574	57	SABm	13.2×5.4	3.79	TRGB	11	SF(*)	7.85	8.24	5.6E7	2.4E8	0.057	8.20	F
NGC3265	1421	E	1.3×1.0	19.6:	TF	6	SF	8.27	8.99	2.8E8	2.6E9	0.38	8.70	B
NGC3351	778	SBb	7.4×5.0	9.33	Ceph	4	SF	8.60	9.19	1.8E9	8.1E9	0.58	10.24	B
NGC3521	805	SABbc	11.0×5.1	11.2	TF	5	SF/AGN(*)	8.39	9.01	6.7E9	3.5E10	1.95	10.69	B

Table 1—Continued

Name ^a	v_H^a (km s ⁻¹)	Morph. ^a	Sizes ^a ($'\times'$)	Dist. ^b (Mpc)	Method ^c	Ref ^d	Nuc. Type ^e	12+log(O/H) ^f		L _{3.6} ^g	L _{TIR} ^h	SFR ⁱ	M _* ^j	PACS/SPIRE ^k
(1)	(2)	(3)	(4)	(5)	(6)	(7)	(8)	(9)	(10)	(L _⊙) (11)	(L _⊙) (12)	(M _⊙ yr ⁻¹) (13)	(M _⊙) (14)	(15)
NGC3621	727	SAd	12.3×7.1	6.55	Ceph	4	AGN	8.27	8.80	1.1E9	7.9E9	0.51	9.38	B
NGC3627	727	SABb	9.1×4.2	9.38	Ceph	4	AGN	8.34	8.99	4.3E9	2.8E10	1.70	10.49	B
NGC3773	987	SA0	1.2×1.0	12.4	TF	6	SF	8.43	8.92	8.8E7	6.8E8	0.16	8.31	B
NGC3938	809	SAC	5.4×4.9	17.9	SNII	16	SF(*)	8.42(+)	9.06(+)	2.7E9	2.0E10	1.77	9.46	B
NGC4236	0	SBdm	21.9×7.2	4.45	TRGB	17	SF(*)	8.17	8.74(+)	1.3E8	5.5E8	0.13	8.36	B
NGC4254	2407	SAC	5.4×4.7	14.4	SNII	16	SF/AGN	8.45	9.13	3.8E9	3.9E10	3.92	9.56	B
NGC4321	1571	SABbc	7.4×6.3	14.3	Ceph	4	AGN	8.50	9.17	5.0E9	3.5E10	2.61	10.30	B
NGC4536	1808	SABbc	7.6×3.2	14.5	Ceph	4	SF/AGN	8.21	9.00	2.2E9	2.1E10	2.17	9.44	F
NGC4559	816	SABcd	10.7×4.4	6.98	TF	5	SF	8.29	8.81	4.4E8	3.3E9	0.37	8.76	F
NGC4569	-235	SABab	9.5×4.4	9.86	TF	18	AGN	8.58(+)	9.26(+)	1.9E9	5.2E9	0.29	10.00	F
NGC4579	1519	SABb	5.9×4.7	16.4	TF	1	AGN	8.54(+)	9.22(+)	6.1E9	1.3E10	1.10	10.02	B
NGC4594	1091	SAa	8.7×3.5	9.08	SBF	19	AGN	8.54(+)	9.22(+)	8.5E9	3.8E9	0.18	11.03	F
NGC4625	609	SABmp	2.2×1.9	9.3	TF	6	SF	8.35	9.05	1.1E8	6.2E8	0.052	8.72	B
NGC4631	606	SBd	15.5×2.7	7.62	TRGB	20	SF(*)	8.12	8.75	1.9E9	2.4E10	1.70	9.76	B
NGC4725	1206	SABab	10.7×7.6	11.9	Ceph	4	AGN	8.35	9.10	4.2E9	8.7E9	0.44	10.52	F
NGC4736	308	SAab	11.2×9.1	4.66	TRGB	21	AGN(*)	8.31	9.01	2.0E9	5.8E9	0.38	10.34	B
DDO154	376	IBm	3.0×2.2	4.3	BS	22	...	7.54	8.02	1.9E6	7.4E6	0.002	6.63	F
NGC4826	408	SAab	10.0×5.4	5.27	TRGB	23	AGN	8.54	9.20	1.8E9	4.2E9	0.26	9.94	F
DDO165	37	Im	3.5×1.9	4.57	TRGB	17	...	7.63	8.04	8.7E6	1.1E7	0.002	7.04	F
NGC5055	504	SAbc	12.6×7.2	7.94	TF	5	AGN	8.40	9.14	3.9E9	2.2E10	1.04	10.55	B
NGC5398	1216	SBdm	2.8×1.7	7.66	TF	1	...	8.35	8.69	5.8E7	3.9E8	0.076	7.79	B
NGC5408	509	IBm	1.6×0.8	4.8	TRGB	24	...	7.81	8.23	3.1E7	1.9E8	0.088	8.29	B
NGC5457	241	SABcd	28.8×26.	6.7	Ceph	4	SF(*)	8.68(B)	...	3.2E9(D)	2.3E10	2.33	9.98	F
NGC5474	273	SACd	4.8×4.3	6.8	BS	25	SF(*)	8.31	8.83	1.2E8	6.1E8	0.091	8.70	B
NGC5713	1883	SABbc	2.8×2.5	21.4	TF	26	SF	8.24	9.03	2.4E9	3.2E10	2.52	10.07	B
NGC5866	692	S0	4.7×1.9	15.3	SBF	2	AGN	8.47(+)	9.12(+)	4.0E9	5.7E9	0.26	10.02	B
NGC6946	48	SABcd	11.5×9.8	6.8	TRGB	27	SF	8.40	9.05	4.0E9	8.6E10	7.12	9.96	B
NGC7331	816	SAb	10.5×3.7	14.5	Ceph	4	AGN	8.34	9.02	8.8E9	5.3E10	2.74	10.56	B
NGC7793	230	SAd	9.3×6.3	3.91	TRGB	28	SF	8.31	8.88	3.1E8	2.3E9	0.26	9.00	B

^aGalaxy name, Heliocentric recession velocity, morphological type, and sizes, as listed in NED, the NASA Extragalactic Database.^bRedshift-independent distance in Mpc.

^cMethods employed to determine the redshift-independent distances. In order of decreasing preference: Cepheids (Ceph), Tip of the Red Giant Branch Stars (TRGB), Surface Brightness Fluctuations (SBF), Supernova Type II Plateau (SNII), flow-corrected Tully-Fisher relation (TF), bright stars (BS), and mean distance to the M81 group (M81G, 3.6 Mpc).

^dReferences to the distances: 1 – Springob, C.M., Masters, K.L., Haynes, M.P., Giovanelli, R., & Marinoni, C. 2009, ApJS, 182, 474; 2 – Tonry, J.L., Dressler, A., Blakeslee, J.P., Ajhar, E.A., Fletcher, A.B., et al. 2001, ApJ, 546, 681; 3 – Van Dyk, S.D., Li, W., & Filippenko, A.V. 2006, PASP, 118, 351; 4 – Freedman, W.L., Madore, B.F., Gibson, B.K., Ferrarese, L., Kelson, D.D., et al. 2001, ApJ, 553, 47; 5 – Tully, R.B., Rizzi, L., Shaya, E.J., Courtois, H.M., Makarov, D.I., & Jacobs, B.A. 2009, AJ, 138, 323; 6 – K.L. Masters, 2005, private communication; 7 – Blakeslee, J.P., Jordan, A., Mei, S., Cote, P., Ferrarese, L., Infante, L. et al. 2009, ApJ, 694, 556; 8 – Saha, A., Claver, J., & Hoessel, J.G. 2002, AJ, 124, 839; 9 – Tully, R.B. 1988, Nearby Galaxy Catalog; 10 – Hoessel, J.G., Saha, A., Danielson, G.E. 1998, AJ, 115, 573; 11 – Dalcanton, J.J., Williams, B.F., Seth, A.C., Dolphin, A., Holtzman, J., et al. 2009, ApJS, 183, 67; 12 – Saha, A., Thim, F., Tamman, G.A., Reindl, B., & Sandage, A. 2006, ApJS, 165, 108; 13 – Karachentsev, I.D., Makarov, D.I., Sharina, M.E., Dolphin, A.E., Grebel, E.K., et al. 2003, A&A 398, 479; 14 – Jones, M.I., Hamuy, M., Lira, P., Maza, J., Clocchiatti, A., Phillips, M. et al. 2009, ApJ, 696, 1176; 15 – Kanbur, S.M., Ngeow, C., Nikolaev, S., Tanvir, N.R., & Hendry, M.A. 2003, A&A, 411, 361; 16 – Poznanski, D., Nathaniel, B., Filippenko, A.V., Ganeshalingam, M., Li, W., et al. 2009, ApJ, 694, 1067; 17 – Karachentsev, I.D., Dolphin, A.E., Geisler, D., Grebel, E.K., Guhatakurta, P., et al. 2002, A&A , 383, 125; 18 – Cortes, J.R., Kenney, J.D.P., & Hardy, E. 2008, ApJ, 683, 78; 19 – Jensen, J.B., Tonry, J.L., Barris, B.J., Thompson, R.I., Liu, M.C., Rieke, M.J., et al. 2003, ApJ, 583, 712; 20 – Seth, A.C., Dalcanton, J.J., & de Jong, R.S. 2005, AJ, 129, 1331; 21 – Karachentsev, I.D., Sharina, M.E., Dolphin, A.E., Grebel, E.K., Geisler, D., et al. 2003, A&A 398, 467; 22 – Makarova, L., Karachentsev, I., Takalo, L.O., Heinaemaeki, P., & Valtonen, M. 1998, A&AS, 128, 459; 23 – Mould, J., & Sakai, S. 2008, ApJ, 686, L75; 24 – Karachentsev, I.D., Sharina, M.E., Dolphin, A.E., Grebel, E.K., Geisler, D., et al. 2002, A&A, 385, 21; 25 – Drozdovsky, I.O., & Karachentsev, I.D. 2000, A&AS, 142, 425; 26 – Willick, J.A., Courteau, S., Faber, S.M., Burstein, D., Dekel, A., & Strauss, M.A. 1997, ApJS, 109, 333; 27 – Karachentsev, I.D., Sharina, M.E., & Huchmeier, W.K. 2000, A&A, 362, 544; 28 – Karachentsev, I.D., Grebel, E.K., Sharina, M.E., Dolphin, A.E., Geisler, D., et al. 2003, A&A, 404, 93.

^eNuclear Type, based on optical spectroscopy: SF=Star Forming; AGN=Non-Thermal Emission. From Table 5 of Moustakas, J., Kennicutt, R.C., Tremonti, C.A., Dale, D.A., Smith, J.D.T., & Calzetti, D. 2010, ApJS, 190, 233; or (*) from Table 4 of Ho, L.C., Filippenko, A.V., & Sargent, W.L.W. 1997, ApJS, 112, 315.

^fCharacteristic oxygen abundances of the galaxies. The two columns, (PT) and (KK), are the two oxygen abundances listed in Table 9 of Moustakas et al. (2010): the PT value, in the left-hand-side column, is from the empirical calibration of Pilyugin & Thuan (2005); the KK value, in the right-hand-side column, is from the theoretical calibration of Kobulnicky & Kewley (2004). (+) Oxygen abundance from the Luminosity-Metallicity relation. For the few galaxies without oxygen abundances in Moustakas et al. only one metallicity value is reported, from: (B) Bresolin, F., Garnett, D. R., & Kennicutt, R. C. 2004, ApJ, 615, 228. (C) Calzetti, D., Harris, J., Gallagher, J.S., Smith, D.A., Conselice, C.J., Homeier, N., & Kewley, L. 2004, AJ, 127, 1405. (E) Engelbracht, C.W., Rieke, G.H., Gordon, K.D., Smith, J.D.T., Werner, M.W., Moustakas, J., Willmer, C.N.A., & Vanzi, L. 2008, ApJ, 678, 804. (P) Pilyugin, L.S., Vilchez, J.M., & Contini, T. 2004, A&A, 425, 849.

^gIntegrated luminosity at 3.6 μm , in units of solar luminosity, expressed as $\nu l(\nu)$, and derived from the fluxes listed in Dale, D.A., et al. (2007), ApJ, 655, 863, and the distances in column (5). (D) Fluxes for NGC3077 and NGC5457 from Dale, D.A., et al. 2009, ApJ, 703, 517. (E) Fluxes for IC342 and NGC2146 from Engelbracht, C.W., et al. 2008, ApJ, 678, 804.

^hTotal infrared luminosity TIR in the 3–1100 μm range, in solar luminosity units. Fluxes are from Spitzer photometry and converted to TIR using equation (4) of Dale & Helou (2002). Fluxes are either from Dale et al. (2007) or from Dale et al. (2009).

ⁱStar Formation Rate ($M_{\odot} \text{ yr}^{-1}$), calculated from the combination of $H\alpha$ and 24 μm luminosity given in Kennicutt et al. (2009). Measurements as listed in Calzetti et al (2010). For NGC5457, the $H\alpha$ luminosity is from Kennicutt et al. (2008) and the 24 micron luminosity from Dale et al. (2009).

^jStellar masses (M_{\odot}) obtained from the multi-color method described in Zibetti et al. (2009), and listed in Skibba et al. (2011). The masses listed in Skibba et al. are rescaled to our updated distance values.

^kPACS and SPIRE observation strategy for each galaxy. The galaxies in the KINGFISH sample have been divided into a bright (B) and faint (F) bin, depending on their Spitzer/MIPS 160 μm surface brightness. The bright bin has median surface brightness $\sim 3 \text{ MJy sr}^{-1}$, while the faint bin has $\sim 1 \text{ MJy sr}^{-1}$. See text for more details.

^lAlthough the mean distance of the M81 Group is used for this galaxy, an unpublished TRGB distance places M81DwB beyond the Group.

Table 2. PACS and SPIRE Imaging Observations

Instrument	Band	PSF FWHM ^a arcsec	Pixel Size ^b arcsec	Sensitivity ^c		
				Bright MJy sr ⁻¹	Faint MJy sr ⁻¹	Parallel MJy sr ⁻¹
PACS	70 μ m	5.76 \times 5.46	1.40	7.1	5.0	11.7
PACS	100 μ m	6.89 \times 6.69	1.70	7.1	5.0	12.3
PACS	160 μ m	12.13 \times 10.65	2.85	3.1	2.2	5.3
SPIRE	250 μ m	18.3 \times 17.0	6.0	1.0	0.7	2.5
SPIRE	350 μ m	24.7 \times 23.2	10.0	0.6	0.4	1.3
SPIRE	500 μ m	37.0 \times 33.4	14.0	0.3	0.2	0.6

^aMajor and minor axis PSF, as taken from PACS and SPIRE Observers’ Manuals. Values correspond to standard KINGFISH scan maps; the PSFs in Parallel mode (IC 342 are slightly degraded, see Observer’s Manuals.

^bPixel sizes for processed data, see §4.

^cAnticipated 1- σ sensitivities per pixel, estimated using HSPOT Version 5. Updated sensitivities will be provided with data products upon delivery.